Laser & Photonics Reviews, March 24, 2012

LASER & PHOTONICS REVIEWS

Abstract The understanding of light-matter interactions at the nanoscale lays the groundwork for many future technologies, applications and materials. The scope of this article is the investigation of coupled photonic-plasmonic systems consisting of a combination of photonic microcavities and metallic nanostructures. In such systems, it is possible to observe an exceptionally strong coupling between electromagnetic light modes of a resonator and collective electron oscillations (plasmons) in the metal. Furthermore, the results have shown that coupled photonic-plasmonic structures possess a considerably higher sensitivity to changes in their environment than conventional localized plasmon sensors due to a plasmon excitation phase shift that depends on the environment.

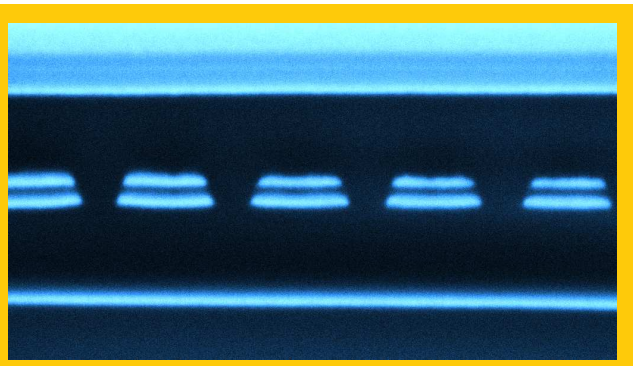

Microcavity Plasmonics: Strong Coupling of Photonic Cavities and Plasmons

Ralf Ameling and Harald Giessen*

1. Plasmon Coupling

1.1. Introduction

The excitation of collective electron oscillations in metallic nanostructures (localized plasmons) or on metal surfaces (surface plasmons) constitutes the basis for the emerging field of plasmonics (Fig. 1). The advances in particle synthesis and nanofabrication offer unique possibilities to produce structures with subwavelength dimensions (metamaterials) with tailored optical properties. Such properties include refractive indices not observed in conventional materials [1] which have lead to many fascinating ideas such as the design of perfect lenses [2] or cloaking devices [3,4]. Further applications include optical nanoantennas [5–7] or, more generally, active and passive components for (integrated) optical devices [8], like high-speed optical switches, tailored optical filters and gratings, nanoscale waveguides as well as coherent optical light sources [9,10]. Furthermore, the technique of surface-enhanced Raman spectroscopy (SERS) has become a widely used method to study molecule spectra that is based on large field enhancements due to the excitation of localized plasmons. The enhanced near-fields of metallic nanoparticles can also be used to detect marginal changes in the environment which is crucial for sensing applications such as the detection of biomolecules [11–13].

In all mentioned fields, plasmonic devices consist of many metallic nanoparticles that interact with each other and the external light field all the time. The different components cannot be regarded as isolated elements, therefore the coupling between plasmons and the coupling of light to plasmons decisively determines the properties and functionality of the applications. So, we have to ask ourselves the following questions: What are the exact coupling mechanisms for different particle distances, especially with respect to three-dimensional geometries? How can we manipulate both coupling strength and range as well as the resonance linewidths, and how can we utilize these modifications to improve plasmonic devices?

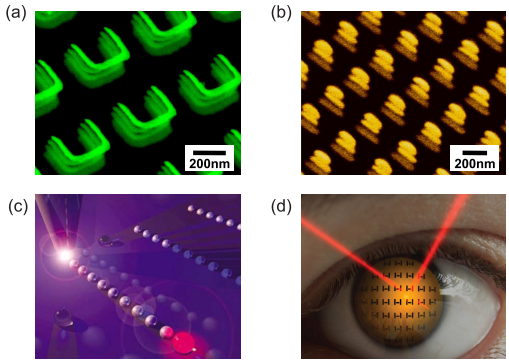

Figure 1 Examples for plasmonic applications: (a) Novel materials [14], (b) nanoantennas [7], (c) waveguides [15], and (d) sensors [16].

Two fundamentally different coupling mechanisms have to be distinguished: coupling via the near-field and coupling via the far-field. Plasmonic nanoparticles can be coupled via their near-fields when the particle distance is substantially lower than the plasmon resonance wavelength of the nanostructure. Many near-field coupled structures have been investigated in the past years [Fig. 2] including nanorod pairs (also referred to as cut-wire pairs) [17,18], nanowire

4th Physics Institute and Research Center SCoPE, University of Stuttgart
* Corresponding author: e-mail: h.giessen@physik.uni-stuttgart.de

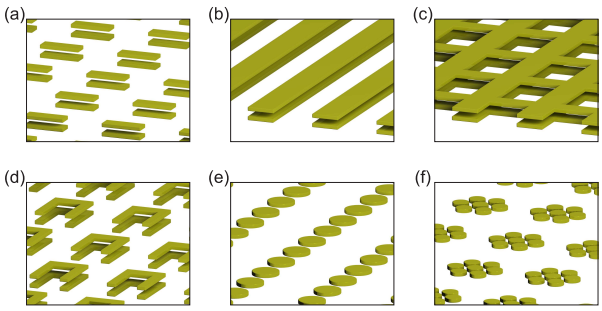

Figure 2 Examples of near-field coupled plasmonic nanostructures: (a) nanorod pairs, (b) nanowire pairs, (c) double-fishnet structures, (d) coupled split-ring resonators, (e) particle chains, and (f) oligomers

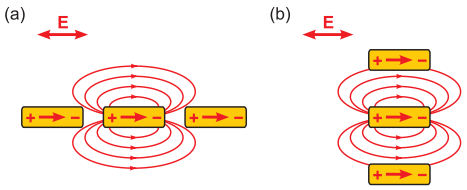

Figure 3 Dipolar electric fields of near-field coupled nanoparticles arranged (a) along and (b) perpendicular to the electric field direction of the incident wave.

pairs [19, 20], double-fishnet structures [21, 22], coupled split-ring resonators [14, 23, 24], particle chains [25, 26], oligomers [27] or clusters of metal particles [28] and metal-dielectric spheres [29]. All near-field coupled plasmonic structures have in common that the fundamental localized plasmon resonance is shifted or split (hybridized) due to the particle interactions. Often, circular currents or currents with opposite directions exhibit magnetic moments that provide a whole new way of interaction and excitation possibilities. In general, the coupling strength decreases when the particle-particle distance increases. When the particle distance, however, approaches or exceeds the wavelength of the plasmon resonances, plasmonic far-field interactions mediated by photonic Fabry-Pérot modes can be observed. This effect can be investigated by analyzing multilayer Bragg stacks of plasmonic structures or plasmonic particles in photonic microcavities. In the context of optical plasmonic nanoantennas [30], far-field coupling has been investigated as well.

This chapter includes an analysis of near-field coupled nanorod pairs and nanowire pairs (simulation and experiment) for their later use in coupled photonic-plasmonic systems. The transition from the near-field to the far-field coupling regime is examined and models to describe the far-field interactions are derived in order to understand the combined photonic-plasmonic systems that will be investigated in the context of strong coupling (Chs. 2 and 3) and sensing applications (Ch. 4).

1.2. Near-Field Coupling

1.2.1. Dipole Model

If the particle size is sufficiently smaller than the particle distance d, the particles can be treated as point dipoles and the plasmonic near-field coupling can be approximated as dipole-dipole coupling [31]. Hence, the distance dependence of the coupling strength is on the order of d^{-3} which has been experimentally demonstrated for example for the case of particle chains [25, 32]. If the resonance wavelengths are large enough, the quasi-electrostatic model (also referred to as Drude model) used for the excitation of localized plasmons in single particles can be applied and retardation effects can be neglected. Two different arrangements of particles can be distinguished (Fig. 3): the particles can be arranged along the direction of the electric field of the incident wave or perpendicular to it. In the first case (Fig. 3a), the restoring force acting on the electrons in the particles is decreased by the dipolar electric field of neighboring particles, resulting in a shift of the localized plasmon resonance to lower frequencies. In the second case (Fig. 3b), the restoring force is increased, leading to a plasmon resonance shift towards higher frequencies. The emitted radiation of the dipoles is mostly directed perpendicular to the oscillation direction. Therefore, in structures aligned perpendicular to the incident electric field, such as stacked nanowires, the coupling is much larger than in a planar arrangement along the electric field.

For more accurate calculations of structures with sizes approaching the particle distance, like in the case of near-field coupled nanorods, the dipole model can be expanded to a series of dipoles representing the currents in a nanostructure of a certain shape. With an appropriate oscillator strength distribution function of the dipoles, good agreement with experimental measurements can be achieved [33]. Despite its deficiencies, the dipole model provides a simple picture to intuitively understand the coupling mechanisms of nanostructures.

1.2.2. Plasmon Hybridization

The second phenomenon that can be observed at coupled nanoparticles besides a mere shift of the plasmon resonances is the resonance splitting. In analogy to the hybridization of atomic energy levels which occurs when the atoms couple and form molecules, localized plasmon resonances can be

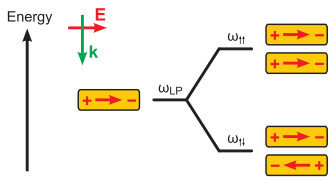

Figure 4 Energy diagram of hybridized localized plasmon resonances in a pair of nanorods.

hybridized [34, 35]. A system of two coupled nanorods, for example, exhibits two different resonances: a symmetric mode where both plasmons oscillate in phase and an antisymmetric mode where the two plasmons oscillate with a phase shift of 180°. The symmetric mode $\omega_{\uparrow\uparrow}$ is located at higher frequencies and the antisymmetric mode $\omega_{\uparrow\downarrow}$ at lower frequencies (Fig. 4). The closer the nanorods approach each other, the larger is the resonance splitting (Fig. 5c). In principle, the antisymmetric (quadrupolar) mode is an optically dark mode, which cannot be excited by an external electromagnetic wave due to the vanishing total electric dipole moment. In order to excite it nevertheless, a structural asymmetry is necessary which is given either by slightly different lengths or by different materials (glass, air) that partially surround the nanorods of a pair. In stacked structures, the spatial variation of the electric field in propagation direction (retardation) enables the excitation of antisymmetric modes. Additionally, the antisymmetric mode exhibits a magnetic moment due to the opposite electric current direction in each pair which constitutes a partial circular current. For this reason, the symmetric and antisymmetric plasmon modes are also often referred to as electric and magnetic plasmon modes since they induce an electric and magnetic dipole, respectively. The interaction with the magnetic field of the electromagnetic wave can lead to many interesting effects. For example, nanorod pairs have been considered as building blocks for materials with a negative index of refraction [18]. It has been extensively discussed whether the magnetic field of the wave is able to directly excite the antisymmetric plasmon modes. A localized plasmon excitation by the magnetic field of an incident electromagnetic wave has been claimed in a number of publications [36, 37]. However, magnetic fields cannot even carry out work. By examination of different spatial arrangements of nanorod pairs, it can be proven [38, 39] that only the electric fields of an incident electromagnetic wave excite symmetric as well as antisymmetric localized plasmon modes.

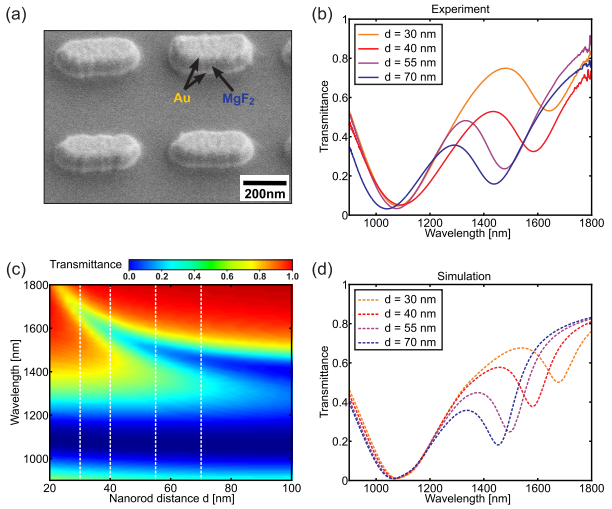

Figure 5 (a) Tilted SEM image of fabricated nanorod pairs. The different Au and MgF_2 layers are clearly visible. Comparison of measured (b) and simulated (d) transmittance spectra of nanorod pairs with different vertical distances d. (c) Simulated transmittance spectra for nanorod distances ranging continuously from 20 nm to 100 nm demonstrating the progression of the symmetric and the antisymmetric plasmon mode. The spectra in (c) correspond to vertical cross-sections of the color plot (d) indicated by dashed white lines.

d	resonance splitting (simulation)	resonance splitting (experiment)
30 nm	597 nm	563 nm
40 nm	507 nm	492 nm
55 nm	429 nm	400 nm
70 nm	390 nm	386 nm

Table 1 Comparison of simulated and measured resonance splittings of pairs of nanorods with different vertical distances d.

1.2.3. Nanorod Pairs

In nanorod pairs, the localized plasmon resonance is hybridized. In Fig. 6, the electric current density in a gold nanorod pair as well as the magnetic field distribution (H_y-component) around the structure was calculated for the symmetric ($\omega_{\uparrow\uparrow}$) and the antisymmetric ($\omega_{\uparrow\downarrow}$) localized plasmon resonance using FDTD simulations [1]. The opposite currents of the antisymmetric mode induce a strong magnetic field between the two nanorods. In the case of the symmetric mode, a weak circular magnetic field around the unidirectional electric current of the nanorod pair can be observed.

The magnitude of the splitting is determined by the coupling strength which can be varied by changing the particle distance. A series of samples of stacked gold nanorod pairs with different vertical distances d ranging from 30 nm to 100 nm was fabricated and compared to FDTD simulations (Fig. 5). The samples were produced on an Infrasil substrate ($n_{sub} = 1.45$) using electron beam lithography with a positive resist procedure. Magnesium fluoride ($n_{MgF_2} = 1.38$) was used as a spacer layer between the nanorods. The length of the nanorods is 320 nm, the width 100 nm and the thickness 30 nm. The unit cell size is 500 nm × 500 nm. The curves demonstrate how the resonance splitting increases when the nanorods approach each other. The experimentally obtained spectra and splitting magnitudes (Tab. 1) agree very well with the simulation. The deviations can be explained with an imprecise measurement of the MgF_2 layer thickness during the evaporation.

1.2.4. Mirror Hybridization

The electrostatic concept of image charges can be used to explain the behavior of a plasmonic nanostructure located

[1] Gold was simulated throughout this article using the quasi-free-electron model with the plasma frequency $\omega_p = 1.31 \cdot 10^{16}$ Hz and the damping frequency $\gamma_e = 1.26 \cdot 10^{14}$ Hz [40–42]

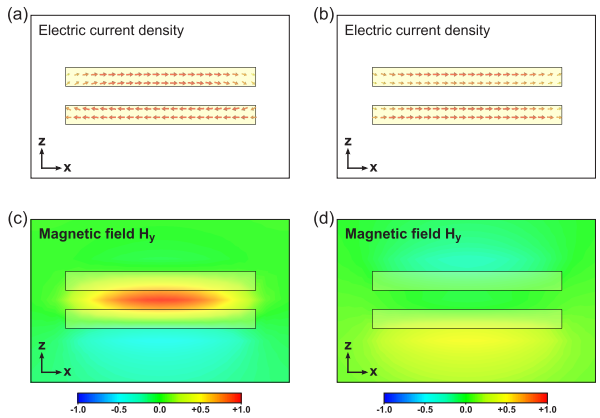

Figure 6 FDTD-Simulation of the electric current density (a,b) and the magnetic field distributions (H_y) (c,d) for the symmetric (a,c) and the antisymmetric (b,d) localized plasmon resonances of a gold nanorod pair.

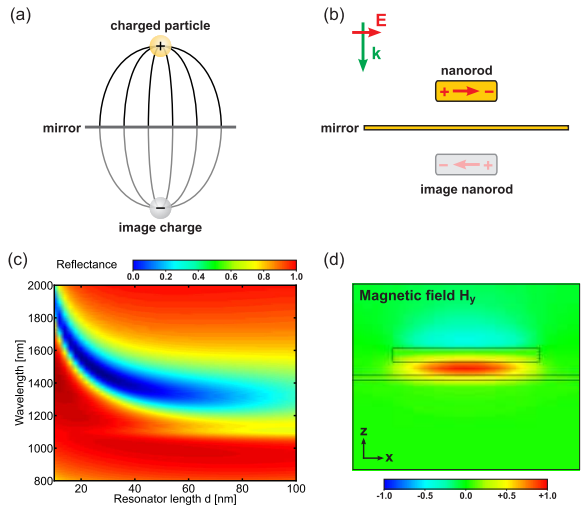

Figure 7 (a) The concept of image charges (b) transferred to plasmonic nanorods. (c) Simulated reflectance spectra for different distances d of the nanorod to the mirror. (d) Magnetic field distribution (H_y-component) at resonance.

close to a mirror. The effects of the mirror on the electric field of a charged particle can be modeled by replacing the mirror with the same particle on the other side of the mirror with opposite charge (image charge) (Fig. 7a). This model can be transferred to plasmonics [43] when a localized plasmon is excited for example in a nanorod that is placed close to a metal layer. Also in this situation, the metal layer can be imagined to be replaced with a second nanorod on the other side of the metal layer with an opposite charge distribution (Fig. 7b). This corresponds to the situation of a nanorod pair where the antisymmetric plasmon mode is excited. Accordingly, a nanorod close to a metal layer exhibits a localized plasmon mode that is shifted to higher energies the further the nanorod approaches the mirror. Fig. 7(c) displays a series of reflectance spectra for different distances d. In analogy to the antisymmetric mode of a nanorod pair (Fig. 6c), a magnetic moment is induced between the nanorod and the mirror (Fig. 7d). The simulated gold nanorods possess the same geometrical parameters as in the previous section. The gold mirror has a thickness of 10 nm. The whole system is simulated in vacuum.

1.3. Far-Field Coupling

1.3.1. Transition from Near- to Far-Field Coupling

All discussed effects so far can be understood by applying the quasi-static approximation and exploring the electric fields. As soon as the particle distance increases and approaches the considered wavelengths, electrodynamic effects such as retardation can no longer be neglected. The nanoparticles start to behave similar to Fabry-Pérot-cavities with resonating mirrors. Fig. 8 displays the characteristics of the resonances of a pair of nanorods when the vertical particle distance is increased from the near-field to the far-field coupling regime. In the near-field coupling regime below $d \approx 200$ nm, the hybridized localized plasmon modes converge to the resonance of a single layer for increasing d. When the distance d exceeds the near-field coupling regime, one observes, instead of a mere vanishing interaction, perturbed Fabry-Pérot-like cavity modes. The perturbation is strongest around the plasmon resonances, indicating a coupling of the plasmons of each layer via the far-field. The vertical coupling of stacked structures has the advantage that the emitted dipole radiation is always directed towards the next dipole. In addition, the phase retardation in the dipole excitation allows the excitation of dark eigenmodes (like the antisymmetric plasmon mode of a nanorod pair) that can not be addressed in a lateral arrangement.

1.3.2. Phase Shift Model

The spectra of the far-field coupled nanorods can be explained by investigating the phase shifts that occur when an electromagnetic wave is propagating through the system.

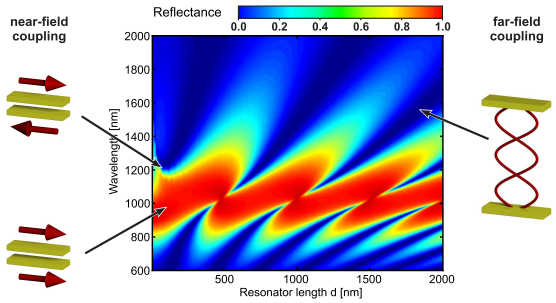

Figure 8 Reflectance spectra for a pair of nanorods with vertical distances, i.e. resonator lengths, d ranging from 10 nm to 2000 nm covering the near- and far-field coupling regimes.

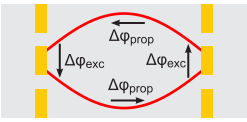

Figure 9 Phase shifts for cavities consisting of nanostructured mirrors.

The resonance condition for any resonator implies that the total phase shift $\Delta\varphi_{\mathrm{tot}}$ that a wave accumulates during one round trip in the resonator has to be a multiple of 2π. In the case of a cavity, this leads to a resonance wavelength of

$$\lambda_{\mathrm{N}} = \frac{2n_{\mathrm{cav}}d}{(N+1) - \frac{\Delta\varphi_{\mathrm{refl}}}{\pi}} \tag{1}$$

with mirror distance d and n_{cav} as the refractive index of the material in the cavity. N is an integer and $\Delta\varphi_{\mathrm{refl}}$ is the phase shift upon reflection at a mirror which is π for a perfect metal. However, this value can deviate significantly from π for real metals and thin metal layers.

If the mirrors of the cavity are replaced with resonating elements, such as plasmonic nanostructures, the phase shift upon reflection $\Delta\varphi_{\mathrm{refl}}$ has to be replaced with the wavelength-dependent phase shift upon plasmon excitation $\Delta\varphi_{\mathrm{exc}}(\lambda)$ (Fig. 9) [2].

To approximate the plasmon excitation phase shift, a simple model of a driven harmonic oscillator can be assumed for the plasmon excitation. It is described by the differential equation

$$\ddot{\vec{r}} + \gamma_{\mathrm{LP}}\dot{\vec{r}} + \omega_{\mathrm{LP}}^2\vec{r} = -\frac{e}{m_{\mathrm{e}}}\vec{E}_0 e^{-i\omega t} \tag{2}$$

with the plasmon damping γ_{LP} and the localized plasmon resonance frequency ω_{LP} of the nanostructure. The field of the incident electromagnetic wave $\vec{E}(t) = \vec{E}_0 e^{-i\omega t}$ acts as a driving force on the electrons in the metal and excites the plasmon. The solution of Eq. 2 leads to

$$\vec{r}(t) = \frac{1}{\omega^2 - \omega_{\mathrm{LP}}^2 + i\gamma_{\mathrm{LP}}\omega}\frac{e}{m_{\mathrm{e}}}\vec{E}(t) \tag{3}$$

In analogy to the quasi-free electron model, a permittivity for the plasmonic layer can now be derived. The plasmonic layer is in this context treated as a homogeneous layer with a permittivity that has a Lorentzian response at the localized plasmon resonance ω_{LP}. This effective permittivity is then given by

$$\varepsilon_{\mathrm{LP}}(\omega) = 1 - \frac{\omega_{\mathrm{p}}^2}{\omega^2 - \omega_{\mathrm{LP}}^2 + i\gamma_{\mathrm{LP}}\omega} \tag{4}$$

with the plasma frequency ω_{p}. To take the influence of a dielectric material with a refractive index n_d in the plasmon layer into account, the non-resonant part of the effective dielectric function $n_{\mathrm{LP}}(\omega)$ can be changed from 1 to n_d. Hence, the refractive index of the plasmon layer is given by

$$n_{\mathrm{LP}}(\omega) = \sqrt{n_d - \frac{\omega_{\mathrm{p}}^2}{\omega^2 - \omega_{\mathrm{LP}}^2 + i\gamma_{\mathrm{LP}}\omega}}\,. \tag{5}$$

Using the Fresnel equations, the reflectivity of such a plasmonic layer embedded between to dielectric layers with the refractive indices n_{cav} and n_{sub} (Fig. 10) can be calculated as

$$R = \frac{R_{12} + R_{23}e^{2ikd}}{1 + R_{12}R_{23}e^{2ikd}} \tag{6}$$

with

$$R_{12} = \frac{n_{\mathrm{cav}} - n_{\mathrm{LP}}}{n_{\mathrm{cav}} + n_{\mathrm{LP}}} \quad \text{and} \tag{7}$$

$$R_{23} = \frac{n_{\mathrm{LP}} - n_{\mathrm{sub}}}{n_{\mathrm{LP}} + n_{\mathrm{sub}}}\,. \tag{8}$$

The phase shift upon plasmon excitation is then given by

$$\Delta\varphi_{\mathrm{exc}} = \arctan\frac{\mathrm{Im}[R]}{\mathrm{Re}[R]}\,. \tag{9}$$

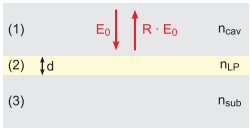

Figure 10 The plasmon layer (2) is treated as a homogeneous layer with an effective permittivity. It is surrounded by two different dielectric materials (1) and (3) representing a substrate and a cavity filling material.

1.3.3. Nanostructured Cavities

The influence of plasmonic excitations on the resonances of cavities consisting of different nanostructured mirrors is investigated in the following. Cavities consisting of nanorods, nanorod pairs and continuous nanowires are compared to a cavity with plane metal layer mirrors.

In Fig. 11(a) the resonances of a cavity consisting of thin gold mirrors can be identified in the reflectance plot. Compared to a cavity with perfect mirrors represented by the dashed white lines ($\lambda_{\mathrm{N}} = \frac{2n_{\mathrm{cav}}d}{N}$), the resonances are shifted due to the penetration depth in the gold layer and due to the effects of reflections on a thin layer. The shift is around $\Delta\lambda \approx 100$ nm at a wavelength of $\lambda = 1000$ nm.

When the metal mirrors are replaced with continuous metal wires (polarization of incident light along the wire), this shift is increased to $\Delta\lambda \approx 200$ nm (Fig. 11b) and can be further increased if less metal is present in the structures

[2] Due to the dispersive nature of metals, also the phase shift upon reflection $\Delta\varphi_{\mathrm{refl}}$ at metal mirrors is wavelength-dependent. However, compared to the phase shift upon plasmon excitation, this dependence is negligibly weak.

forming the cavity. Structure sizes smaller than the wavelength cause effects that have to be explained in terms of effective structure parameters like in this case an effective metal density resulting in an effective mirror thickness and a corresponding reflection phase shift that shifts the cavity resonance accordingly.

For the case of two layers of plasmonic nanostructures with a large distance, the phase shift model is applied to calculate the resonances (Eq. 9). For nanorods, the results are displayed as continuous white lines in the colored reflectance plots of Fig. 11(c). The model can accurately reproduce the simulated spectra for nanorod cavities. Fitting parameters are the plasmon damping parameter γ_{LP} and the localized plasmon resonance frequency ω_{LP}. When approaching the localized plasmon resonance (indicated by the horizontal dashed black line), the linewidth of the Fabry-Pérot modes is extremely decreased. Here, the spatial arrangement of the emitters matches their emission wavelength, and the phase behavior is strongly modified. This large perturbation due to the strong phase dependence of the cavity resonances in this region will later be explored for plasmon sensing applications (Ch. 4).

In the case of two far-field coupled nanorod *pairs* (Fig. 11d), the additional influence of the hybridized plasmon modes can be observed. Besides the bending of the resonances around the symmetric plasmon resonance, additional perturbations around the antisymmetric plasmon resonance can be observed.

The following geometric parameters were used for the simulations: The thickness of the plane metal mirrors is 10 nm, the continuous nanowires have a thickness of 30 nm and a width of 100 nm. The nanorods have a length of 300 nm, a width of 100 nm and a thickness of 30 nm. The distance between the two nanorods of a pair is 40 nm. The unit cell size is 500 nm $\times$ 500 nm. The mirrors and nanostructures consist of gold, the surrounding medium of all systems is vacuum including the interior of the cavities.

The simulated spectra could accurately be reproduced experimentally [44] for the case of two layers of stacked nanowires by a series of fabricated samples covering the near- and far-field coupling regime.

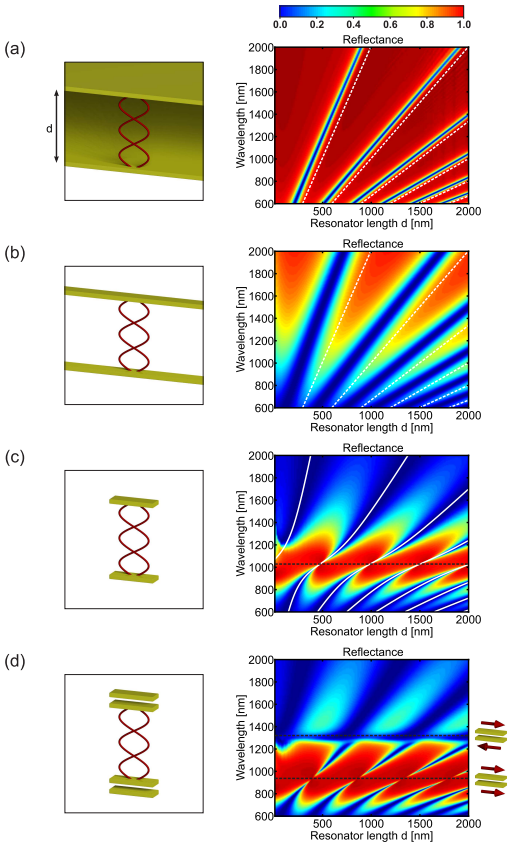

Figure 11 Reflectance spectra of nanostructured cavities with varying resonator length d. The cavity mirrors are formed by (a) plane metal layers, (b) continuous nanowires, (c) nanorods, and (d) nanorod pairs. The dashed white lines in (a) and (b) indicate the resonances for a cavity with perfect mirrors, the solid white lines in (c) indicate the resonances when the phase shift model is applied. The black lines in (c) and (d) correspond to the localized plasmon resonances of a single layer of nanorods and nanorod pairs.

1.3.4. Multilayer Stacks

In order to proceed towards an understanding of three-dimensional materials made of plasmonic nanostructures, multilayer stacks of plasmonic nanorods and nanowires have been simulated. The color plots in Fig. 12 show the resonances of five layers of nanorods compared to five ordinarily coupled cavities. In general, each cavity resonance is split into N modes in the case of N coupled cavities. Thinner metal layers lead to a better coupling of the cavities and therefore to a larger splitting. Extensive treatments of coupled cavities can be found in the context of metal-dielectric stacks (or one-dimensional photonic crystals), for example in [45].

For a medium consisting of several layers of nanostructures that are coupled vertically via their far-field, a combination of the effects of coupled multilayer mirror cavities (Fig. 12a) and a two-layer far-field coupled nanorod cavity (Fig. 11c) can be observed. First, the resonances are split with the splitting magnitude being dependent on the effective density of the plasmon layer determined by the thickness and shape of the nanostructures. The number of split modes is determined by the number of coupled cavities. The formation of band gaps already takes place at a very small number of cavities which can be attributed to the relatively long plasmon lifetime. The cross-sections in Fig. 12 point out the formation of band gaps for a five layer structure. The second effect is the perturbation of the modes around the plasmon resonance frequency. By tuning the plasmon resonance (via the nanorod length) and the layer distance, these kind of structures offer the possibility to fabricate materials with tailored reflection and transmission properties using only a small number of stacked layers.

For the simulations, the same geometric and material parameters as in Sec. 1.3.3 were used. The simulated results

could be confirmed experimentally with a structure consisting of four layers of stacked continuous nanowires [46].

2. Strong Coupling of Photonic and Localized Plasmon Modes

2.1. Introduction

Microcavities confine the electromagnetic field within a very small volume and allow large field enhancement [47–52]. When combined with radiating species, such as atoms [53], molecules [54–57], or semiconductor excitons [58], strong coupling between the optical modes of the microcavity and resonant modes of the emitters can occur. This strong coupling has been utilized in the past to demonstrate enhancement and inhibition of spontaneous emission [59, 60] or to tailor the photon statistics [61]. Also vacuum Rabi-splitting of excitons in quantum dots has been observed [62, 63]. An additional feature of microcavities is their ability to couple two radiating systems via the optical far-field over a larger distance [64, 65] (see also Sec. 1.3.3).

In this chapter, strong coupling between localized plasmons in nanorod pairs and photonic modes of a microcavity is presented [66]. Furthermore, it is demonstrated that the field symmetry of the microcavity modes can excite symmetric and antisymmetric localized plasmon modes in a nanorod pair that are associated with electric and magnetic dipoles. The coupling strength depends on the nanorod position in the microcavity. The design allows especially strong coupling of light to the generally weakly excited magnetic dipole and can serve as a model for far-field coupling of localized particle plasmons in individual layers of stacked metallic metamaterials [67, 68]. The work accounts for a better understanding of the coupling of multiple localized plasmons in three-dimensional metamaterials [14, 69].

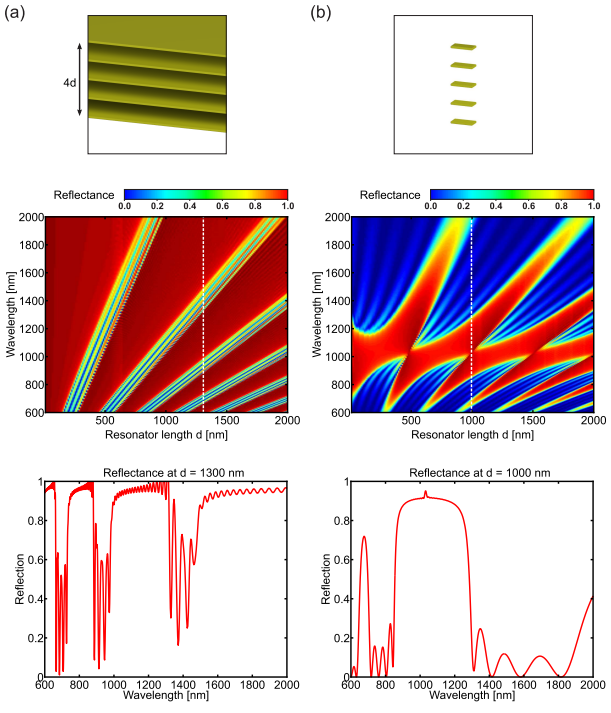

Figure 12 Reflectance plots of multilayer cavities consisting of (a) plane metal layers and (b) metal nanorods. The graphs correspond to cross-sections in the color plots indicated by the dashed white lines.

2.2. Strong Coupling

2.2.1. Strong Coupling of Quantum Emitters and Light

In the past, strong coupling between photons and many different emitters has been observed. In 1992, it was the first time that mode-splitting due to the strong coupling of a photonic cavity mode to a two-level atom has been observed [53]. In that experiment, a cavity is tuned in such a way that it has the same resonance frequency as the atomic transition (Fig. 13). To obtain then a periodic energy exchange between the cavity mode and the atom, there are three important factors that play a key role:

- the coupling strength g of the electric field to the atom which is proportional to the electric field inside the cavity and to the dipole moment of the excited atom state,
- radiation losses at the mirrors κ_M,
- losses due to spontaneous emission of the atom in any direction κ_E.

When two modes of the same energy are coupled, the modes are split around the common resonance frequency ω_0. In the spectrum, the coupling strength g determines the extent of the splitting. The irreversible decay channels κ_M and κ_E describe the ways a photon can leave the coupled

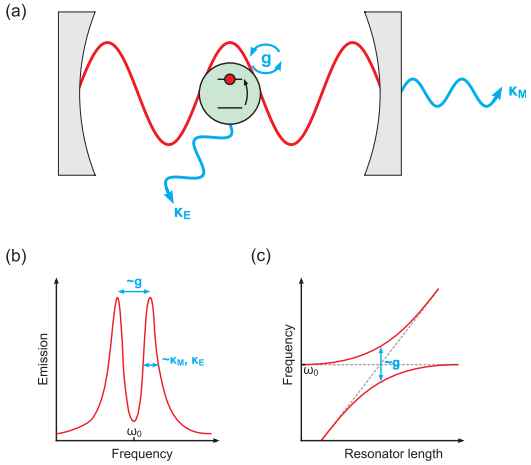

Figure 13 (a) Strong coupling of a two-level atom in a cavity with the coupling strength g and the irreversible decay channels at the mirrors κ_M and due to spontaneous emission κ_E. (b) Splitting of the resonances around the resonance frequency of the emitter ω_0. (c) Anticrossing behavior of the resonances when the cavity resonance is detuned around the emitter resonance.

atom-cavity state and determine the linewidth of the resonances. If g is large in comparison, then a mode-splitting can be observed and strong coupling is achieved.

In Tab. 2, some experimental results of the last years are compared. Besides atoms, the same effects can be observed for any quantum emitter, also for quantum dots or quantum wells. Instead of a classical cavity, one can also use a photonic crystal with a photonic band gap, Bragg-mirrors, or metal layers. A measure for the quality of a coupling experiment is the relation of the splitting energy and the spectral linewidth. For atoms, values up to 5 have been achieved, for quantum dots, the best measured value so far is 2.2.

Emitter	Cs-Atom	InAs QD	InGaAs QD	GaAs QD
Cavity type	Mirrors	Photonic Crystal	Micro-pillars	Micro-disk
Splitting / Linewidth	5	1.3	0.7	2.2
Date of experiment	2004 [70]	2004 [63]	2004 [62]	2005 [71]

Table 2 Comparison of different systems exhibiting Rabi-splitting [72] (QD = quantum dot).

2.2.2. Transition to Plasmonic Systems

The transition of the concept of strong coupling between photonic cavity modes and an emitter to plasmonic systems is straightforward. Instead of the Rabi-splitting for the atoms, which is a quantum effect, now the classical polariton splitting of the plasmons occurs. The atom-field coupling strength becomes the plasmon field coupling strength which is proportional to the plasmon dipole moment and the electric field. Also, radiation losses at the mirrors play a role: in the regarded structures, thin gold metal layers were used as mirrors. Finally, κ_E corresponds to the dephasing rate of the plasmons associated with the damping frequency of the metal. The investigated coupled photonic-plasmonic system consists of an array of gold nanorods or nanorod pairs located inside a microcavity that is made out of a dielectric material surrounded by two gold layers that act as the mirrors (Fig. 14). This coupled photonic-plasmonic system can be described with the Hamiltonian

$$H = \begin{pmatrix} E_N & g \\ g & E_{LP} \end{pmatrix} \tag{10}$$

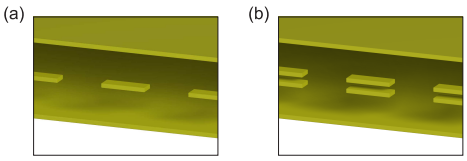

Figure 14 (a) Nanorods and (b) nanorod pairs in a microcavity constitute a strongly coupled photonic-plasmonic system.

with the energy of the N-th photonic cavity mode $E_N = \hbar\omega_N$, the energy of the localized plasmon mode $E_{LP} = \hbar\omega_{LP}$, and the coupling constant g. The solution of the equation

$$H\Psi = \begin{pmatrix} E_N & g \\ g & E_{LP} \end{pmatrix} \begin{pmatrix} \psi_N \\ \psi_{LP} \end{pmatrix} = E \begin{pmatrix} \psi_N \\ \psi_{LP} \end{pmatrix} \tag{11}$$

with the eigenstate of the polariton Ψ being composed of the eigenstates of the cavity ψ_N and the plasmon ψ_{LP} yields the dispersion of the coupled system. At the point where E_N equals E_{LP}, this results in a mode splitting of $2g$.

2.3. Single Nanorods in a Microcavity

At first, a layer of single nanorods is placed into the center of a microcavity (Fig. 15). The geometric parameters of the nanorods are again 300 nm × 100 nm × 30 nm (length × width × thickness) with an array unit cell size of 500 nm × 500 nm. To compare the simulated spectra with experimental measurements, the simulated material parameters were adjusted to the fabricated samples. This means the cavity is filled with a dielectric with the refractive index $n_d = 1.40$ and is surrounded by a substrate with $n_{sub} = 1.45$ on the lower side and by air on the upper side. The mirrors as well as the nanorods themselves are made out of gold. The localized plasmon resonance wavelength of the isolated nanorod (in the dielectric medium) is in this case $\lambda_{LP} = 1480$ nm.

The resonances of an empty cavity appear as straight lines in the color-coded reflectance plot of Fig. 15 and are here indicated by black dashed lines and their mode numbers N. The localized plasmon eigenmode is indicated by the horizontal white dashed line. When the resonance wavelengths of the cavity are close to the plasmon resonance of the nanorod, the described polariton splitting can be observed. A closer look reveals that only the odd cavity modes ($N = 1, 3, 5, ...$) are influenced. They show a huge anticrossing with a splitting of several hundred nanometers whereas the even modes ($N = 2, 4, 6, ...$) remain completely unperturbed.

The mode splitting is proportional to the coupling strength g which is proportional to the electric field strength.

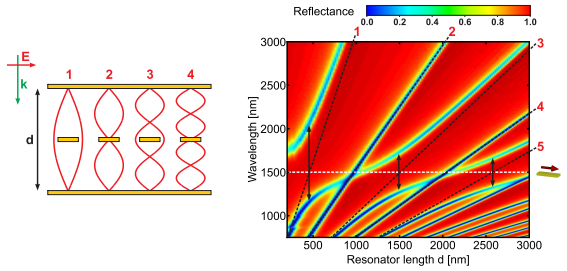

Figure 15 Single nanorods in a microcavity and the corresponding reflectance plot for different wavelengths and resonator lengths. The dashed white and black lines correspond to the unperturbed plasmon and cavity modes. Around every second intersection of the modes, an anticrossing is observable (indicated by black arrows).

Hence, the behavior of the modes can be explained by regarding the symmetry of the electric fields in the cavity: For the odd modes, there is an electric field anti-node located in the center of the cavity where the nanorods are located. This means the field strength at these positions is very high leading to a large interaction and therefore a strong coupling of the photonic cavity mode to the plasmon. For the even cavity modes, the situation is totally different. Here, we have an electric field node in the center of the cavity. This means that the field is close to zero at the position of the nanorods. Hence, the plasmons cannot be excited, no interaction can take place, and the modes remain unaffected.

2.4. Nanorod Pairs in a Microcavity

2.4.1. Electric and Magnetic Coupling

Very interesting effects occur when the single nanorods are replaced by nanorod pairs [66] (Fig. 16b). In addition to the symmetric plasmon mode of the nanorod pair, the antisymmetric mode can interact with the cavity modes. The plasmonic structure can now exhibit two different resonances and Eq. 11 has to be extended to

$$H\Psi = \begin{pmatrix} E_{\mathrm{N}} & g_{\uparrow\uparrow} & g_{\uparrow\downarrow} \\ g_{\uparrow\uparrow} & E_{\uparrow\uparrow} & 0 \\ g_{\uparrow\downarrow} & 0 & E_{\uparrow\downarrow} \end{pmatrix} \begin{pmatrix} \psi_{\mathrm{N}} \\ \psi_{\uparrow\uparrow} \\ \psi_{\uparrow\downarrow} \end{pmatrix} = E \begin{pmatrix} \psi_{\mathrm{N}} \\ \psi_{\uparrow\uparrow} \\ \psi_{\uparrow\downarrow} \end{pmatrix} \qquad (12)$$

with the indices $\uparrow\uparrow$ and $\uparrow\downarrow$ denoting the symmetric and antisymmetric localized plasmon resonance.

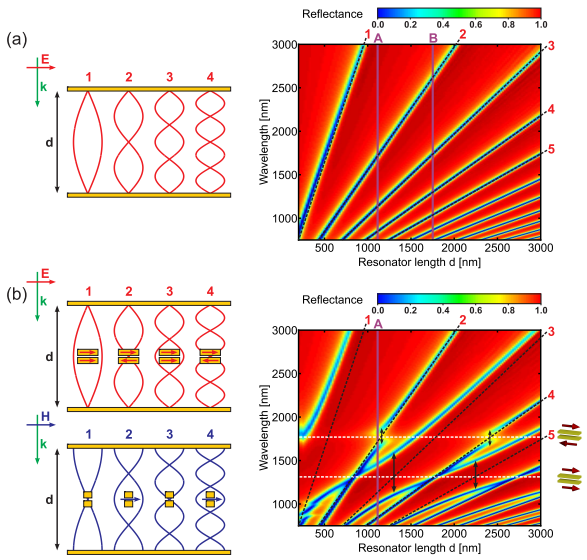

Figure 16 (a) Empty microcavity and (b) nanorod pairs in a microcavity with the corresponding reflectance plots for different wavelengths and resonator lengths. The dashed white and black lines correspond to the unperturbed plasmon and cavity modes. The mode splitting is indicated by the black arrows. The vertical violet lines (marked A and B) denote the positions of the fabricated samples (see Sec. 2.4.4).

In the considered case, the two nanorods are separated by a 40 nm thick spacer with the refractive index $n_{\mathrm{MgF_2}} = 1.38$. All other material parameters are the same as in the previous section. The resonance wavelengths of an isolated nanorod pair are then $\lambda_{\uparrow\uparrow} = 1320$ nm for the symmetric and $\lambda_{\uparrow\downarrow} = 1760$ nm for the antisymmetric plasmon mode.

The modifications of the resonances in the reflectance plots of Fig. 16b explain what is going on in this coupled system: The odd modes are only split around the resonance wavelength of the symmetric plasmon mode whereas the even modes are only split around the resonance wavelength of the antisymmetric plasmon mode. In the center of the resonator, the electric field vectors of the odd modes point into the same direction for both nanorods of a pair, so only the symmetric mode can be excited. The field amplitude is close to the maximum for the odd modes near the nanorod spatial region, therefore also the coupling $g_{\uparrow\uparrow}$ is strong. The even modes, however, possess an electric field node directly in between the two nanorods, resulting in opposite directions of the electric field vector for each nanowire, exciting only the antisymmetric mode. Since the field amplitude is low around the node, the strong coupling between the even modes and the plasmon $g_{\uparrow\downarrow}$ is less pronounced. One might also look at the interaction from a magnetic viewpoint [73]. The magnetic field in the microcavity is maximum at the nodes of the electric field. Hence, the interaction with the antisymmetric (magnetic) nanorod pair modes is then strongest at such locations.

2.4.2. Variation of Plasmon Position

To verify the explanations of the previous section, the nanorod pairs are placed at different positions in the cavity. The nanorods are positioned in such a way that the ratio of the distances to the two gold cavity mirrors are $d_1 : d_2 = 1 : 2$ and $1 : 3$. When placed around an electric field node of the third cavity mode (Fig. 17a), this mode can couple only to the antisymmetric plasmon mode and not to the symmetric plasmon mode anymore. The other cavity modes couple only to the symmetric mode. Similar observations apply for nanorod pairs placed around the electric field node of the fourth cavity mode (Fig. 17b).

2.4.3. Nature of the Modes

The field plots in Fig. 18 provide a deeper insight concerning the nature of the split modes. In a nanorod pair, the electric fields in the nanorods point in the same direction for the symmetric and in opposite directions for the antisymmetric plasmon mode (see Fig. 6). The coupling of the third resonator mode to the symmetric plasmon mode is illustrated in Fig. 18a and b. The electric field points into the same direction in both nanowires, whereas it points into opposite directions for the coupling of the second resonator mode to the antisymmetric plasmon mode in Fig. 18c and d. Note that the two split resonances of one microcavity mode differ in such a way that the plasmon oscillation is

in phase with the microcavity mode for the resonance at the lower wavelength and antiphase for the resonance at the higher wavelength. Fig. 18e and f finally shows magnetic fields that belong to the third cavity mode and the corresponding strong magnetic dipoles that are exhibited by the antisymmetric plasmon modes. For the split mode with the lower wavelength, the induced magnetic dipole oscillates in phase with the magnetic field of the cavity mode, for the split mode with the higher wavelength, the magnetic dipole oscillates antiphase.

2.4.4. Fabrication Details

The samples were fabricated using physical vapor deposition for the metals and the magnesium fluoride (MgF_2) spacer layers, spin coating for the thick dielectric layers in the microcavity, and electron beam lithography for the nanostructuring. With these techniques the investigated structures can be manufactured in a layer-by-layer fashion. First, a 20 nm thick gold layer serving as the lower mirror is evaporated on an Infrasil glass substrate that has been coated with 3 nm chromium for a better adhesion of the gold. Thereafter, the first dielectric spacer between the gold-layer and the later nanorods is spin-coated. For the spacer we use the polysiloxane-based spin-on glass IC1-200 in different mixing ratios with butanol, resulting in different layer thicknesses. The spacer consists of one or more dielectric coating layers with different mixing ratios. Subsequently, the positive resist is spun onto the sample in which the nanorod pattern is written by electron beam lithography. After the exposure and the development, the sample is coated with 30 nm Au, 40 nm MgF_2, and 30 nm Au. By leaving the sample in acetone for several hours, the unexposed PMMA

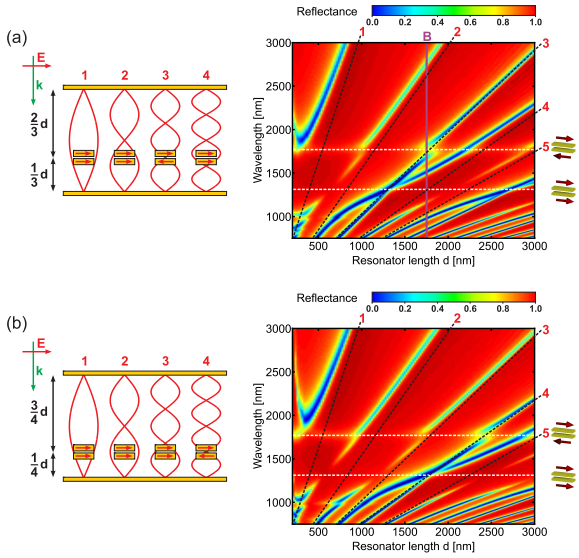

Figure 17 Nanorod pairs in a microcavity placed at an electric field node of the (a) third and (b) fourth cavity mode including the corresponding reflectance plot for different wavelengths and resonator lengths. The dashed white and black lines correspond to the unperturbed plasmon and cavity modes. The vertical violet line (marked B) denotes the positions of the fabricated sample (see Sec. 2.4.4).

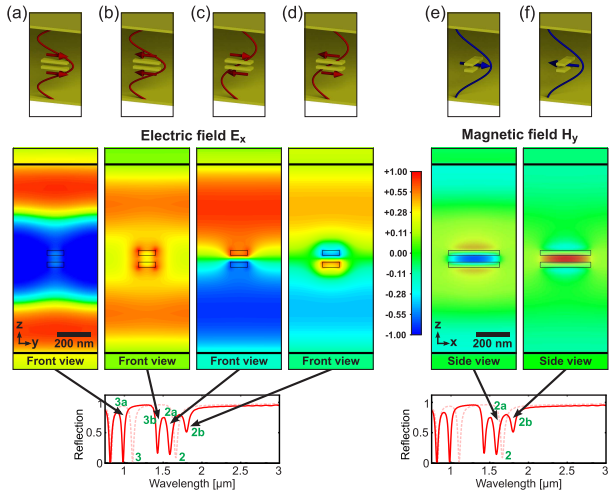

Figure 18 © American Chemical Society [66]. Plots of the electric (a-d) and magnetic (e,f) field distributions (logarithmic color scale) at the various resonances of a pair of nanorods in a microcavity. (a) and (b) show the x-component of the electric field in the y-z-plane for the third cavity mode (3) that is split in two modes (3a and 3b) due to strong coupling to the symmetric plasmon mode. (c) and (d) show the same field for the second cavity mode (2) that is split in two modes (2a and 2b) due to strong coupling to the antisymmetric plasmon mode. The reflectance spectra below corresponds to cross-sections (marked A) of the color plots in Fig. 16a and b. The solid lines denote the reflectance of nanorod pairs in a microcavity, the dashed lines show the unperturbed modes of an empty cavity (compare with Fig. 20). (e) and (f) show the y-component of the magnetic field of the split second resonator mode (2) in the x-z-plane.

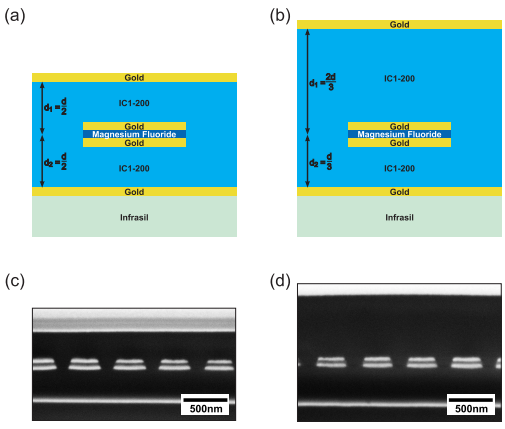

Figure 19 © American Chemical Society [66]. (a, b) Sketches of the two fabricated samples A and B. (c, d) SEM-images of focussed ion beam cuts of the two samples providing a side view on the different layers.

as well as the gold and magnesium fluoride layers thereon are removed (lift-off), and only the nanorod pairs on the dielectric coating remain. The period of the nanorod array is 500 nm in both directions, the length of the rods is around 300 nm, the width 100 nm. For planarization a 100 nm thick layer of IC1-200 and subsequently the upper dielectric spacer is spun on the sample. Finally, 20 nm gold is evaporated forming the upper mirror of the cavity.

Two samples (A and B) have been produced in the above explained manner (Fig. 19) to confirm the simulated results experimentally. One sample (A) has been produced with the nanorod pairs located in the center of the resonator. The resonator length of sample A is 1100 nm. This is approximately the length where the second resonator mode wavelength equals the antisymmetric plasmon mode wavelength. By regarding the reflectance plot in Fig. 16(b), one recognizes that both kind of splittings (around the symmetric and around the antisymmetric plasmon mode) should be visible in a measured spectrum at this position. In the second sample (B) the nanorod pairs are positioned in such a way that the ratio of the distances to the two gold cavity mirrors is $d_1 : d_2 = 1 : 2$. The total resonator length is 1740 nm. Around this length, the wavelength of the third resonator mode equals the antisymmetric plasmon mode wavelength. From Fig. 17(a) one can expect to see a coupling of the third resonator mode to the antisymmetric plasmon mode and of the fourth resonator mode to the symmetric plasmon mode under these conditions.

2.4.5. Experimental Results

Each measured reflection spectrum of a fabricated sample (Fig. 20) corresponds to one cross-section in the color-coded reflectance plots of Figs. 16 and 17a (marked as vertical violet lines A and B). Additional reflection spectra were recorded away from the structure to measure the unperturbed resonance modes and thus determine the resonator length. The reflection and transmission spectra have been measured with a Fourier transform infrared spectrometer using a Si-diode and an MCT-detector and linearly polarized light.

The measured spectrum of sample A is in good agreement with the simulation (Fig. 20a). Around $\lambda_{\uparrow\downarrow} = 1760$ nm, the splitting of the second mode (2) into two peaks (2a, 2b) around the antisymmetric plasmon mode can be clearly observed. Additionally, the large splitting of the third mode ($3 \rightarrow$ 3a, 3b) due to its strong coupling to the symmetric plasmon mode is evident. Finally, the higher modes remain mostly unaffected for this resonator length. The relative difference in the strength of the modes in experiment and simulation can be explained by the fact that the thickness of the spacer layers between nanorod pair and metal mirror is subject to variations.

Sample B has a resonator length of 1740 nm. Around this length, the wavelength of the third resonator mode (3) equals the antisymmetric plasmon mode wavelength. Due to the non-central position of the nanorod in the cavity, strong coupling between the third mode and the antisymmetric plasmon mode evident through a large mode splitting can be observed (see Fig. 20b). The strong coupling of the fourth mode (4) to the symmetric plasmon mode can also be seen in the measured spectrum characterized by a splitting into two well-separated peaks (4a and 4b). The second resonator mode (2) does not split up for this resonator length and is only slightly shifted.

2.4.6. Splitting Energies

The splitting of the modes is determined by the strength of the coupling. As pointed out in Sec. 2.2.1, strong coupling is achieved when the ratio of the splitting and the linewidth of the modes is larger than 1. In Tab. 3, the simulated and measured splitting wavelengths and energies, as well as the ratios of the splittings over the linewidths are compared for the different coupled modes. The simulated splitting values are taken at resonator lengths corresponding to those of the fabricated samples (Sec. 2.4.4). These resonator lengths do not always correspond exactly to the values where the unperturbed plasmon and cavity modes would intersect. The splitting energies simulated around the exact crossing of the modes are slightly smaller (see Fig. 16b): for the coupling to the symmetric plasmon mode, a splitting energy of 354 meV (38 % of resonance energy) was simulated, for the coupling to the antisymmetric mode the corresponding value was 82 meV (12 % of resonance energy), both for the structure with the nanorod pair in the center of the cavity. For the off-central position of the nanorod pairs, slightly smaller values were determined. All measured and simulated ratios of the splitting energy and the linewidth of the resonances are larger than 1 (up to 8.9 for the symmetric coupling). Therefore, strong coupling of photonic and localized plasmonic modes has been demonstrated for all studied structures.

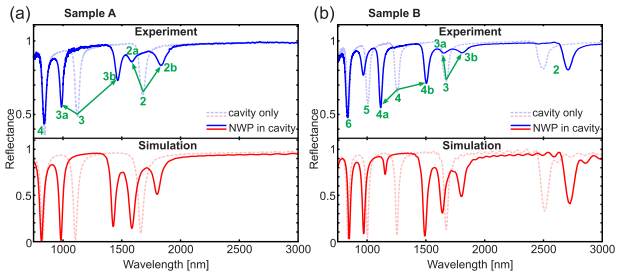

Figure 20 © American Chemical Society [66]. Comparison of measured and simulated reflection spectra. (a) Sample A: Nanorod pair in a central position in the resonator ($d_1 = d_2 =$ 550 nm). (b) Sample B: Nanorod pair in a non-central position in the resonator ($d_1 = 580$ nm, $d_2 = 1160$ nm). The dashed lines in the background correspond to the reflectance spectra of an empty cavity.

2.5. Multilayer Nanorods in a Microcavity

Finally, the effects of multiple layers of nanorods in a cavity are investigated. In agreement with Sec. 1.3.4, the splitting of each mode into a number of modes corresponding to the number of subcavities can be observed (Fig. 21). However, in contrast to the case without limiting mirrors on the upper and lower side, the resonances remain well-separated and do not start to form band gaps. Here, the effect of the cavity of allowing only resonances at well-defined frequencies can be observed. In the case of nanorod pairs in a cavity, also the interaction with the antisymmetric plasmon mode manifests itself as small anticrossings around the plasmon resonance frequency.

$d_1 : d_2$	Coupled modes	Splitting energy	$\frac{\text{Splitting energy}}{\text{Resonance energy}}$	$\frac{\text{Splitting}}{\text{Linewidth}}$
1:1	↑↓ to 2	94 meV (108 meV)	13% (15%)	2.7 (2.5)
1:1	↑↑ to 3	392 meV (410 meV)	42% (44%)	8.9 (8.0)
1:2	↑↓ to 3	68 meV (63 meV)	10% (9%)	2.0 (1.5)
1:2	↑↑ to 4	244 meV (288 meV)	26% (31%)	6.7 (6.5)

Table 3 Mode splitting of nanorod pairs in a microcavity at different positions. d_1 and d_2 are the distances of the nanorods to the lower and upper cavity mirror. The coupled plasmon modes are indicates by ↑↑ (symmetric) and ↑↓ (antisymmetric), the coupled cavity modes are defined by their mode number N. The numbers in brackets are the measured values.

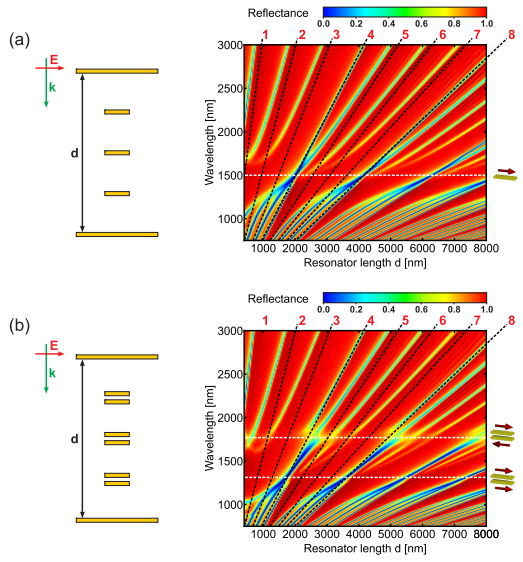

Figure 21 Reflectance plots of three layers of (a) single nanorods and (b) nanorod pairs in a microcavity for different resonator lengths d. Black and white dashed lines denote the unperturbed resonances of cavities and nanorods / nanorod pairs.

To understand the features of the resonances in more detail, it is again helpful to look at the symmetry of the electric fields of the cavity modes. The cavity modes with $N = 4, 8, 12, ...$ possess electric field nodes at the positions of the single nanorods and in between two nanorods of a pair. This means on the one hand that the field strength is very low at the positions of the single nanorods, therefore no interaction takes place and the corresponding cavity modes remain unperturbed and appear as straight lines in Fig. 21a. On the other hand, in the case of nanorod pairs, the electric field points into different directions for each nanorod of a pair, therefore the antisymmetric plasmon mode can be excited and small mode splittings appear around the antisymmetric plasmon resonance in Fig. 21b.

All other modes have non-vanishing electric fields at the positions of the nanorods, so they can interact with the symmetric plasmon mode and show quite pronounced anticrossings around the single nanorod and the symmetric nanorod pair resonance.

3. Strong Coupling of Photonic and Surface Plasmon Modes

3.1. Introduction

In this chapter, strong coupling of *surface* plasmon modes on a thin metal layer via localized plasmons of nanowires to photonic microcavity modes is investigated [74]. In analogy to the previous chapter, a modified environment is created by a photonic microcavity which manipulates the coupling strength of light to localized and surface plasmons and influences the plasmon resonances. In particular, an array of nanowires is placed close to a mirror, and a second mirror is positioned near Bragg distance. The distance has to be accurately controlled, since strong coupling can only be observed when the resonances of the photonic microcavity and the plasmons intersect. The coupling becomes evident from an anti-crossing of the resonances when the cavity resonance is detuned around the plasmon resonances. The resonant modes of the coupled system are experimentally determined for different resonator lengths by applying external pressure to the microcavity while recording the spectra. Excellent agreement with simulations is achieved.

Furthermore, it is demonstrated that a strong plasmon-plasmon interaction over far-field distances can be achieved by placing a second layer of nanowires also close to the opposite mirror of the cavity. The far-field interaction, which is mediated by the photonic microcavity modes, causes a splitting of both the localized and the surface plasmon modes.

3.2. Structure Geometry and Coupling Scheme

3.2.1. Excitation of Surface and Localized Plasmons

In an isolated continuous metal nanowire, localized plasmons can be excited when the incident light is polarized

perpendicular to the wire. The localized plasmon resonance wavelength λ_{LP} is determined by the width and thickness of the wire as well as the material parameters of the metal and the dielectric environment.

Placing a thin metal layer near an array of nanowires has two effects (Fig. 22a). First, in analogy to electrostatics, the effects of a mirror close to a charged particle is equal to the effect of an image charge placed on the opposite side of the mirror with opposite charge (see Sec. 1.2.4). Hence, the system of a nanowire placed closely above a mirror resembles very much the system of a pair of stacked nanowires where the antisymmetric plasmon mode (magnetic mode) is excited [43, 75, 76]. Depending on the distance of the wire to the mirror, the resonance wavelength is shifted towards higher wavelengths. Using a dielectric spacer of 30 nm with a refractive index of $n = 1.38$ between wire and mirror and a mirror thickness of 15 nm, the localized plasmon resonance is shifted to $\lambda_{LP} = 1050$ nm for nanowires with a thickness of 20 nm and a width of 140 nm. In the same manner as for a nanowire pair, a magnetic dipole is induced for a nanowire close to a mirror.

The second effect is the grating-induced excitation of propagating surface plasmons on the metal-substrate interface [77, 78]. For the used parameters, a nanowire period of $p_x = 600$ nm allows surface plasmons with a resonance wavelength of $\lambda_{SP} = 880$ nm (Fig. 22b). By plotting the magnetic fields, the two resonances can be identified (Fig. 22c).

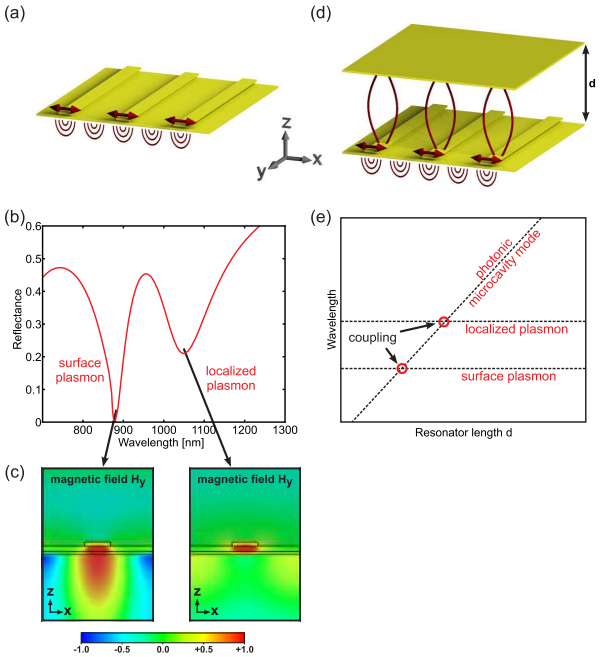

Figure 22 © Optical Society of America [74]. (a) In an array of metal nanowires close to a thin metal layer localized and surface plasmons can be excited (b). (c) The magnetic field plots of the two resonances reveal the nature of the two plasmon modes. (d) By adding a second metal layer, the microcavity modes can couple to the plasmon modes for those mirror distances d where the microcavity modes intersect with plasmon modes (e). The red lines in the structure illustrations indicate the standing electric fields. Illumination is from below with polarization along the x-direction.

3.2.2. Enhancing Light-Plasmon Coupling by a Photonic Microcavity

In order to obtain strong coupling of light to the plasmon modes, a microcavity is formed by positioning a second mirror at a distance d to the nanowires (Fig. 22d). The mirror consists of a 100 nm thick gold layer. When the distance d is varied, a strong interaction with the plasmon modes is expected each time when the cavity resonance is equal to a plasmon resonance (Fig. 22e). From a magnetic point of view, the cavity modes can be coupled very effectively to the magnetic plasmon modes due to their strong magnetic field (anti-nodes) near the mirrors. The mode coupling causes an anti-crossing of the resonances and can be observed in the simulated reflectance plot of Fig. 25a. The simulations were performed using a Fourier model based Maxwell solver [79–81].

3.2.3. Fabrication and Measurement Technique

The experimental realization of this structure has been accomplished as follows: First, a gold layer and a magnesium fluoride layer ($n_{MgF_2} = 1.38$) are evaporated on a glass substrate ($n_{sub} = 1.45$). The nanowires are fabricated by electron beam lithography using a positive resist procedure with a final lift-off. Fig. 23 displays a top and side view of the fabricated structure. The second mirror is evaporated on a second glass substrate which is then turned around and pressed

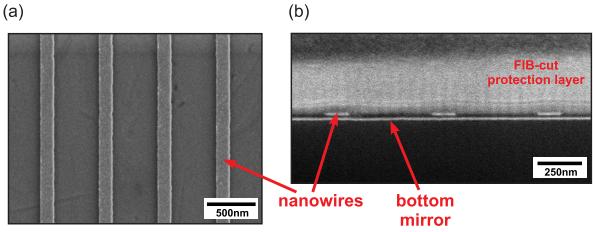

Figure 23 © Optical Society of America [74]. Scanning electron microscope image of the structure. (a) Top view and (b) side view obtained by a focussed ion beam cut.

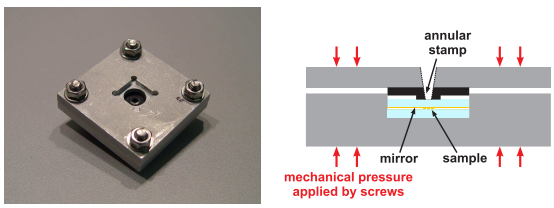

Figure 24 Setup used to press the mirror onto the sample.

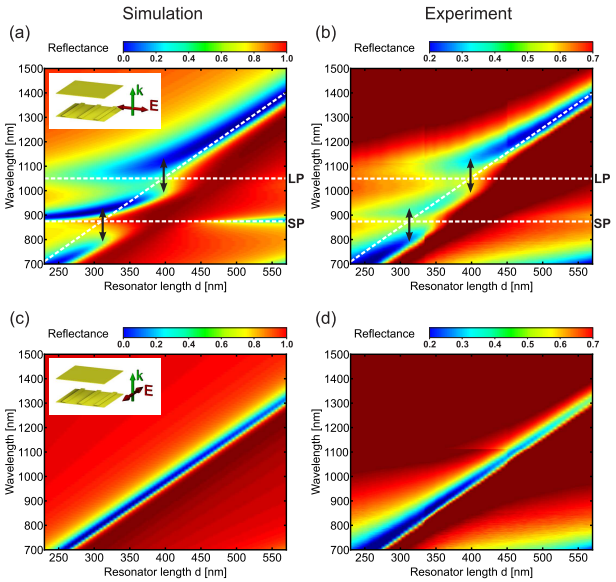

Figure 25 © Optical Society of America [74]. (a,c) Simulated and (b,d) measured reflectance for different microcavity lengths d. For incident light polarized perpendicular to the nanowires (a,b), the anticrossings of the modes caused by the strong coupling of the plasmons to the cavity modes can be observed (indicated by black arrows). The white dashed lines denote the localized plasmon (LP) and surface plasmon (SP) resonances as well as the unperturbed cavity resonance. For incident light polarized along the continuous nanowires (c,d), only the cavity modes are excited.

onto the nanowire array. The pressure is applied via a small annular stamp around the region where the nanowire array with a total size of 700 µm × 700 µm is written (Fig. 24). Using this technique, the microcavity length can be tuned from several micrometers to only a few hundred nanometers by simply changing the mechanical pressure. By placing the whole device in a Fourier-transform infrared spectrometer with an attached infrared microscope, the behavior of the resonances of the system can be measured by recording the reflected light for a series of different microcavity lengths. The reflectance plot that was experimentally obtained in this way (Fig. 25b) corresponds very well to the simulated one.

In order to determine the actual distance of the mirrors, the polarization is turned by 90°. This way, the incident light is polarized along the continuous nanowires. Hence, no plasmons can be excited and only the unperturbed cavity resonances are detected (Fig. 25c and d). It has to be taken into account that a certain apparent length increase of the cavity occurs [82, 83], since the reflection phase shifts of the light on the metal layers is slightly larger than π. By comparing to simulations, this apparent length increase has been determined as $\delta_{\parallel} = 90$ nm for polarization along the nanowires. For polarization perpendicular to the nanowires, the phase shift upon reflection is different due to the additional resonant plasmon excitation resulting in an apparent length increase of $\delta_{\perp} = 128$ nm. The relation between the first order resonance of the cavity λ_1, the mirror distance d, and the apparent length increase δ is given by $\lambda_1 = 2(d + \delta)$.

3.2.4. Mode Splitting

In Fig. 26, the simulated and experimentally determined reflection spectra are plotted for two different cavity lengths $d_{SP} = 310$ nm and $d_{LP} = 395$ nm. At these distances, the resonance wavelength of the cavity corresponds to the surface plasmon and the localized plasmon resonances and the splitting energies can be directly observed. The reflectance spectra (red curves) correspond to cross-sections of Fig. 25 at the positions indicated by the black arrows. For comparison, the unperturbed plasmon resonances are plotted in the graphs as well (dashed gray curves). The simulated magnitudes of the splittings are 131 nm for the surface plasmon and 126 nm for the localized plasmon which correspond to splitting energies of 224 meV and 141 meV. Experimentally, slightly smaller splittings were measured: 122 nm for the localized plasmon and 119 nm for the surface plasmon resonance. These values are quite large and correspond to splitting/resonance energy ratios of about 1:10 indicating strong coupling.

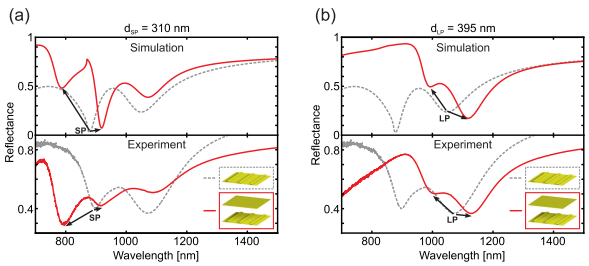

Figure 26 © Optical Society of America [74]. Simulated and measured reflectance spectra (red curves) at those cavity lengths where the resonance wavelength of the microcavity corresponds to the (a) surface plasmon (SP) and (b) localized plasmon (LP) resonances. The dashed gray curves in the background correspond to the unperturbed plasmon resonances of the structure without the second mirror.

3.3. Cavity-Assisted Far-Field Interactions

Photonic cavity modes can mediate far-field coupling of emitters. This concept can also be applied to couple plasmons via the far-field (see Sec. 1.3). By positioning a second layer of nanowires close to the second mirror of the cavity (Fig. 27a), a coupled photonic-plasmonic system is created which allows the interactions of the plasmons on one side of the cavity with the plasmons on the other side. The thickness of both mirrors is now 15 nm, all other parameters are the same as in the previous section.

The coupling causes an additional splitting both of the surface plasmon and the localized plasmon modes. On the reflectance plot for different cavity lengths d (Fig. 27b), the

additional splittings occur around the unperturbed plasmon modes each time when a cavity resonance frequency equals a plasmon resonance frequency. On the magnetic field plots (Fig. 27c), the nature of the different modes is revealed. The surface plasmon splits into a symmetric mode $\omega_{SP}^{\uparrow\uparrow}$ and an antisymmetric mode $\omega_{SP}^{\uparrow\downarrow}$ with the surface plasmons on the two sides of the cavity oscillating in phase or anti-phase. The same can be observed for the localized plasmons.

The symmetry of the electric field in the cavity determines which of the split plasmon modes exhibits the higher and which one the lower resonance frequency. For an interaction with the first cavity mode (and all subsequent odd cavity modes), the electric field points in the same direction for both sides of the cavity. Therefore, the localized plasmons on both sides of the cavity are preferably excited in phase inducing magnetic moments that point in opposite directions ($\omega_{SP}^{\uparrow\downarrow}$ and $\omega_{LP}^{\uparrow\downarrow}$). At a slightly higher frequency, the plasmons oscillate antiphase inducing magnetic moments pointing in the same direction ($\omega_{SP}^{\uparrow\uparrow}$ and $\omega_{LP}^{\uparrow\uparrow}$). For the second (and all subsequent even cavity modes), the situation is exactly inverted. The marked positions (1-4) in Figs. 27b and c belong to the second cavity mode, therefore the antisymmetric plasmon resonances $\omega_{SP}^{\uparrow\downarrow}$ and $\omega_{LP}^{\uparrow\downarrow}$ are located at lower wavelengths and the symmetric plasmon resonances $\omega_{SP}^{\uparrow\uparrow}$ and $\omega_{LP}^{\uparrow\uparrow}$ at higher wavelengths.

The values for the mode splitting in the simulations are 25 nm for the surface plasmon and 80 nm for the localized plasmon. These splittings are only observable when the damping parameter is reduced, therefore an experimental realization of the far-field coupled plasmons could not yet be achieved.

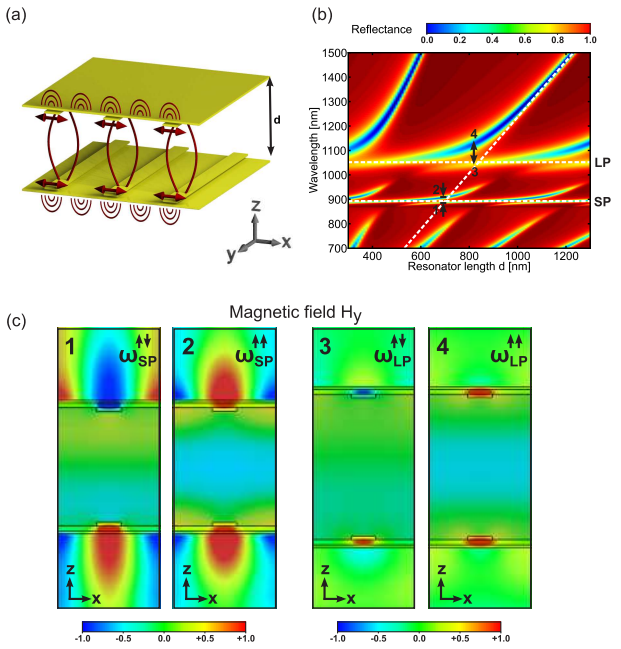

Figure 27 (a) Nanowires located close to both mirrors of the cavity allow surface and localized plasmon far-field coupling mediated by the cavity. (b) Reflectance plot for different cavity lengths d. The white dashed lines denote the unperturbed plasmon and cavity resonances. (c) Magnetic field plots of the split resonances at the positions (1-4) marked in the reflectance plot.

4. Cavity-Enhanced Plasmonic Sensing

4.1. Introduction

In this chapter, a method to enhance the sensing properties of a localized plasmon sensor using a microcavity is presented [84]. At first, the general idea of localized plasmon resonance sensing is reviewed and different methods to characterize a sensor are presented. Subsequently, the new concept to enhance these kind of sensors is introduced. It is based on the combination of localized plasmons in nanostructures and a photonic microcavity. Metal nanorods that are placed near Bragg distance above a metal mirror form a Fabry-Pérot microcavity and constitute a coupled photonic-plasmonic system.

The localized plasmon resonances of the nanorods and the phase shifts upon plasmon excitation are extremely sensitive to changes in the refractive index of the material surrounding the nanorods. Compared to the plasmonic nanorods alone, the coupled photonic-plasmonic system allows for a much more sensitive detection of small refractive index changes. The field distributions as well as the dependence on the unit cell size and the incident angle are analyzed. Finally, experimental results with water and glucose solutions that are channeled over a fabricated sample using a special sensing cell are presented.

4.2. Localized Plasmon Resonance Sensing

4.2.1. General Principle

One of the most prominent features of plasmonic nanostructures in terms of practical applications is their use as localized surface plasmon resonance (LSPR) sensors [11–13].

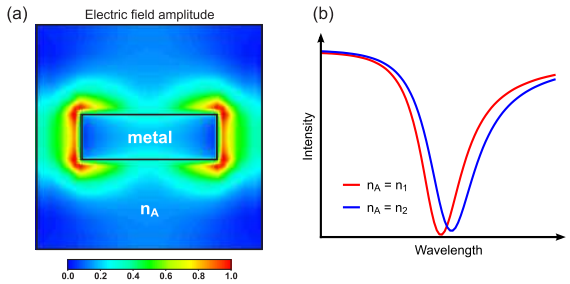

Figure 28 The principle of LSPR sensing: (a) the total time averaged electric fields of an excited plasmon in a nanostructure, here a nanorod, outreach the metal, therefore (b) the resonance frequency of a plasmonic nanostructure depends on the refractive index n_A of the surrounding medium.

The spectrum of sensing applications implies medical demands such as the detection of biomolecules [85–88], safety-related concerns such as the measurement of gas concentrations [89,90] as well as monitoring chemical reactions [91]. In all mentioned areas, the detection of small quantities preferably down to single molecules is desired. Therefore, all sensors have to be evaluated with respect to their sensitivity upon marginal changes of the environment. Localized plasmon resonances in metallic nanostructures have the potential to provide these properties [92].

The electric fields of the localized plasmons surround the nanostructures which associates the spectral position of the resonances to the refractive index of the environment [93,94] (Fig. 28). An increase in the refractive index n_A of the surrounding medium causes a redshift of the plasmon resonance. These spectral shifts can be detected and give information about changes in the analyte. By a functionalization of the nanoparticle surfaces, the sensitivity can be extended from a mere detection of refractive index changes towards selective detection of a certain molecule concentration [95,96].

Besides localized plasmon resonances, also propagating surface plasmon resonances can be used for sensing [97]. The obtained sensitivities are generally higher but due to the more difficult excitation of surface plasmon modes, these concepts require rather complex experimental setups.

4.2.2. Structure Dependence

The magnitude of the spectral shift is very dependent on the structure geometry. In Fig. 29 the plasmon resonance shifts of different geometric structures are compared [3]. The more symmetric a structure is, the smaller is the plasmon resonances shift. While nanospheres and nanocubes are among the least sensitive structures, more complex geometries like nanobipyramids and nanobranches exhibit very large shifts. At those complicated structures with rather sharp edges, the amount of electric field outside the nanostructure is much higher than for simple structures like nanospheres. The sensitivity of nanorods lies between the complex and the very symmetric structures.

To demonstrate the concept of enhancing the sensitivity of a certain plasmonic nanostructure, we chose nanorods mainly due to their relatively easy fabrication using electron beam lithography. The aspect ratio (length divided by width) of a nanorod has a big influence on the sensitivity. The optimal aspect ratio for sensitive nanorods has been determined to be between 3 and 4 [94].

4.2.3. Characterization of Sensing Properties

Comparing sensitive structures using only their sensitivity S defined as the plasmon resonance shift $\Delta\lambda$ divided by the refractive index change Δn is not always adequate. Depending on the regarded spectral region and on the detection methods, the sensitivity of a structure is not a sufficient measure to define its sensing properties. The absolute wavelength and the linewidth of the resonance are also crucial factors for a sensor. Therefore, a figure of merit FOM is defined [99] as the sensitivity S divided by the full width at half maximum $FWHM$ of a Lorentz-shaped resonance. Since the detection of the spectral shift of a resonance requires a spectrometer, a more practical way of detection that will be used in biosensors is the measurement of the reflected or transmitted light intensity for one particular wavelength (Fig. 30) using for example a laser diode. To take this into account, a new sensitivity usually referred to as S^* can be defined as the intensity variation ΔI for a given refractive index change Δn. Furthermore, the absolute intensity is a substantial factor because small intensity variations are much easier to detect when the overall intensity is already low. Therefore, a new figure of merit FOM^* is defined [94,100] as the sensitivity S^* divided by the absolute intensity I. According to this, the various definitions of the sensing capabilities of a given

[3] The data is taken from Chen et al. [98] and is based on measurements of gold nanoparticles of different shape and size in different concentrations of glycerol in water.

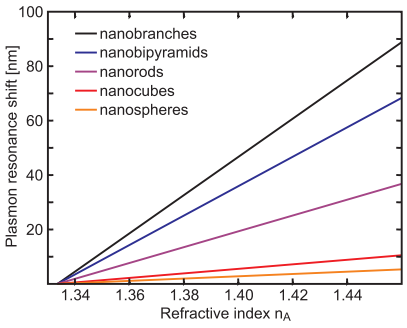

Figure 29 Dependence of the plasmon resonance shift on the particle shape [98].

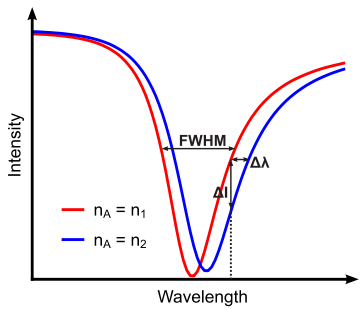

Figure 30 Spectral shifts $\Delta\lambda$ as well as the variations of the transmitted or reflected intensity ΔI can be detected.

structure are specified as follows:

$$S = \frac{\Delta\lambda}{\Delta n} \tag{13}$$

$$S^* = \frac{\Delta I}{\Delta n} \tag{14}$$

$$FOM = \frac{S}{FWHM} \tag{15}$$

$$FOM^* = \frac{S^*}{I}. \tag{16}$$

In order to obtain high values for these parameters, it is required to have resonances that exhibit not only a large spectral shift but possess also a small linewidth and a large modulation depth.

4.3. Cavity-Enhanced Sensing

4.3.1. Linewidths and Sensing Principle

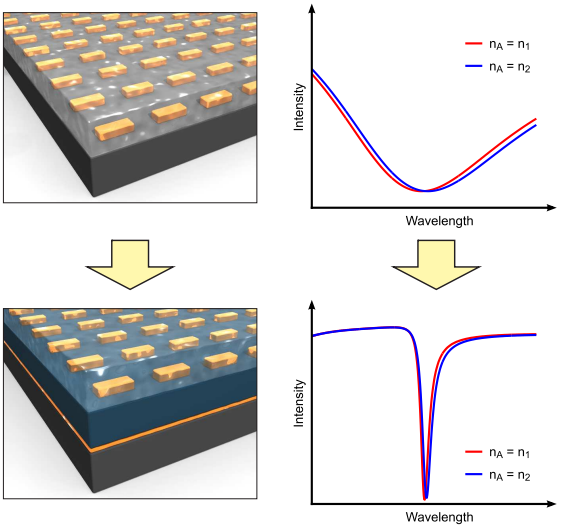

Figure 31 Decreasing the linewidth of a localized plasmon resonance by coupling to a photonic microcavity.

As pointed out in the previous section, the large linewidth of plasmon resonances is a major problem because it impairs the sensing properties fundamentally. A plasmon resonance of a nanorod in the near-infrared region, for example, has a linewidth of typically a few hundred nanometers resulting in a very low Q-factor. This is a big drawback because for any practical applications large intensity variations of the reflected or transmitted light at a certain wavelength are desired.

The reason for the large linewidth of plasmon resonances is the strong radiative damping of the metal [101]. An effective way of decreasing the linewidth is to couple the plasmon to a system with a narrow resonance. This concept has already been applied successfully in the context of the plasmonic analog of electromagnetically induced transparency (EIT) [102–105] where a broad plasmonic dipole is coupled to a narrow plasmonic quadrupole resonance. The resulting structure exhibits sharp peaks and superior sensing properties.

In a similar way, the plasmonic resonances can be coupled to a photonic microcavity [106] (see also Ch. 2). Here, the linewidth of the coupled photonic-plasmonic resonance arises from the *cavity* Q-factor due to the modified photonic density of states and hence the modified radiative damping rate. As a result, the idea of a combination of plasmonic nanostructures with a Fabry-Pérot microcavity provides a way of decreasing the linewidth of the resonances and therefore improving the sensing properties of nanostructures (Fig. 31).

4.3.2. Phase Shifts

The sensitivity of the coupled photonic-plasmonic structure arises from a strong phase dependence of the localized plasmon excitation in the nanorods (Fig. 32) which can be explained with a simple effective medium model accounting for the phase shifts. In analogy to Sec. 1.3.2, the total phase shift that a wave accumulates during one round trip in the cavity is the sum of the phase shifts due to the propagation of the wave through the cavity $\Delta\varphi_{\text{prop}}$, the phase shifts upon reflection at the cavity mirrors $\Delta\varphi_{\text{refl}}$, and the phase shifts that occur on plasmon excitation $\Delta\varphi_{\text{exc}}$. The resonance condition for the cavity sensing structure is then given by

$$\Delta\varphi_{\text{tot}} = 2\Delta\varphi_{\text{prop}} + \Delta\varphi_{\text{refl}} + \Delta\varphi_{\text{exc}} = (N+1)\cdot 2\pi\,. \tag{17}$$

This leads to the expression

$$\lambda_N = \frac{2n_{\text{cav}}d}{(N+1) - \frac{1}{2\pi}\left(\Delta\varphi_{\text{refl}} + \Delta\varphi_{\text{exc}}(n_A)\right)} \tag{18}$$

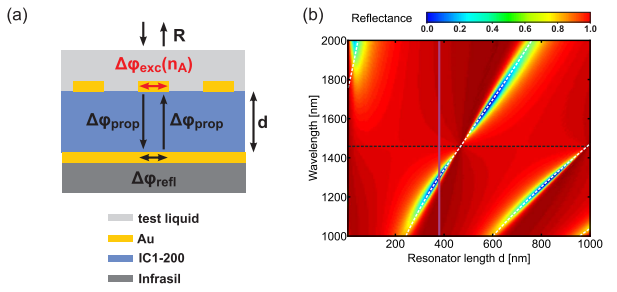

Figure 32 Nanorods combined with a cavity: (a) Phase shifts and (b) reflectance plot for different wavelengths and distances. The vertical violet line represents the fabricated sample, the dashed white lines denote the calculated resonances using Eq. 18, the dashed black line is the unperturbed localized plasmon resonance of the nanorods.

for the resonance wavelengths λ_N of the whole system with n_{cav} being the refractive index of the material in the cavity and d the distance between the mirror and the nanorod array. The phase shift upon reflection at the mirror $\Delta\varphi_{refl}$ can be calculated using the Fresnel equations. The plasmon excitation phase shift $\Delta\varphi_{exc}$ is dependent on the refractive index of the analyte n_A and can be calculated using the driven harmonic oscillator model with the assignment of an effective permittivity to the nanostructured layer using Eq. 9 with the corresponding refractive indices for the analyte n_A and the cavity n_{cav}.

This way, the phase shifts become dependent on the refractive index n_A of the material surrounding the nanostructure. A change in this refractive index causes a shift of the localized plasmon resonance wavelength λ_{LP} of the nanorod. Therefore, the phase shift upon plasmon excitation $\Delta\varphi_{exc}$ is changed. As a result, the total phase shift is changed and the resonance condition (Eq. 17) for the cavity is no longer fulfilled for the same wavelength. Due to the small linewidth, a slight spectral shift of the resonance causes a large intensity variation ΔI. The reflected light intensity at the former minimum is therefore now substantially different from zero. This results in large values of the sensitivity S^* and the figure of merit (Sec. 4.4.4) when the nanorods are placed at around Bragg distance to the mirror (Sec. 4.3.3). The calculated resonances using Eq. 18 agree very well with the simulated reflectance plot in Fig. 32b.

4.3.3. Optimal sensing structure parameters

The largest changes in $\Delta\varphi_{exc}$ can be obtained when the resonance of the coupled system (white dashed line in Fig. 32b) is close to the plasmon resonance of the nanorod (black dashed line in Fig. 32b). However, exactly at the plasmon resonance the reflected light intensity is equal to 1 since no light is transmitted by the nanorods array under this condition. Therefore, no resonance can be observed here. The ideal wavelength for sensing is about 10% above or below the plasmon resonance wavelength.

The distance of the nanorods to the mirror then has to be near Bragg distance ($d_{Bragg} = \frac{N\lambda}{2}$). Under these conditions, the largest enhancement of the sensitivity S^* and the figure of merit FOM^* can be observed (Fig. 33). The actual deviations from the exact Bragg distance are due to reflection phase shifts at the mirror and at the nanorod layer that are not equal to π. Applying Eq. 18 leads for the regarded wavelength of $\lambda = 1300$ nm to a matching resonator length of $d = 380$ nm which agrees very well with the experiments (see Sec. 4.4.4). The highest observed value for the sensitivity S^* is 6.1. Zero reflectance in simulations (see Fig. 39a) leads to an infinite FOM^* for the resonance wavelength.

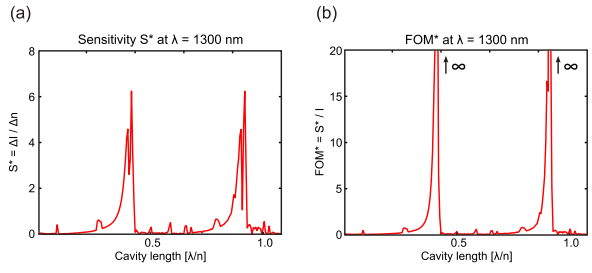

Figure 33 © American Institute of Physics [84]. Sensitivity S^* and figure of merit FOM^* calculated from simulations for materials with refractive indices $n_1 = 1.33$ and $n_2 = 1.37$ surrounding the nanorods. The values are enhanced when the nanorods are placed around Bragg distance to the mirror.

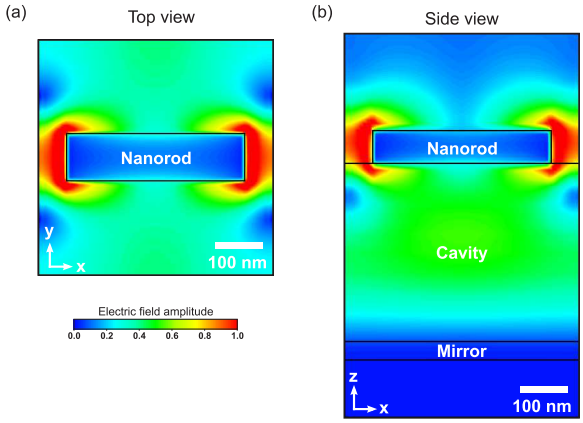

Figure 34 © American Institute of Physics [84]. Distribution of the time-averaged total electric field in the sensor structure. The (a) top view and (b) side view of a unit cell reveal the strong field localization at the nanorod ends and in the cavity.

For the simulations, nanorods with a length of 380 nm, a width of 100 nm, and a thickness of 70 nm were used. The unit cell size is 500 nm × 500 nm, the thickness of the mirror is 40 nm. The refractive indices of the substrate, the spacer and the analyte are $n_{sub} = 1.45$, $n_{IC1} = 1.40$, and $n_{H_2O} = 1.33$, respectively.

4.3.4. Field Localization

The field distributions in Fig. 34 for a cavity length of $d = 380$ nm point out the concentration of the electric fields at the nanorod ends and inside the cavity at the resonance wavelength of $\lambda = 1300$ nm. Due to the strong field localization between the nanorods, the sensing volume is very small. Only where the electric fields outreach the structure, a change in the environment can have an influence on the plasmon resonance. A functionalization of the nanorod ends can make the localized sensor selective for only a certain kind of molecules which is favorable for biochemical or medical applications. Additionally, the field localization inside the cavity might be utilized for sensing which would further increase the structure's sensitivity. This could be achieved by using porous media or by placing the nanorods on pillars. Further improvements include a combination of the cavity structure with micro- and nanofluidic techniques [88, 107].

4.3.5. Unit Cell Size and Incident Angle

In this section, the effects of changing the lateral distance between the nanorods and of changing the angle of the incident light are investigated. In Fig. 35, the periods in x- and y-direction p_x and p_y are varied and the reflectance for each period is plotted around the resonance of the combined cavity-nanorod structure.

Changing p_x does not affect the resonance of the system unless the distance between two nanorods is less than about 120 nm which means in this case a period in x-direction smaller than 500 nm. However, the system resonance is very dependent on the period in y-direction. By enhancing p_y from 200 nm to 700 nm, the resonance wavelength is shifted from 1160 nm to 1420 nm. This behavior can be explained by regarding the dipole emission patterns of the nanorods [see Sec. 1.2.1]. In oscillation direction (x-direction) almost no radiation is emitted which means that an interaction to neighboring nanorods can only take place via the near-field. Most radiation is emitted perpendicular to the nanorod (in y-direction). In resemblance to cavities consisting of nanorods (Sec. 1.3.3), the resonance wavelength is very dependent on the nanorod distance. Although the variations in the resonances are quite remarkable, the principle of the sensor remains valid also for large unit cells. Therefore, in principle only one element can be used for the detection of very small quanta which, in combination with the strong field localization, justifies the designation as localized sensor.

The dependence of the resonances on the incident angle of light θ is plotted in Fig. 36. For incident angles of less than 10°, no changes can be observed. For larger incident angles, the resonances are shifted towards lower wavelengths until the system breaks down at around $\theta = 40°$ and other effects like Rayleigh-Wood anomalies dominate the behavior of the sensor. The large independence on the incident angle is useful for many possible applications.

For the simulations, the same structure parameters as in Sec. 4.3.3 are used.

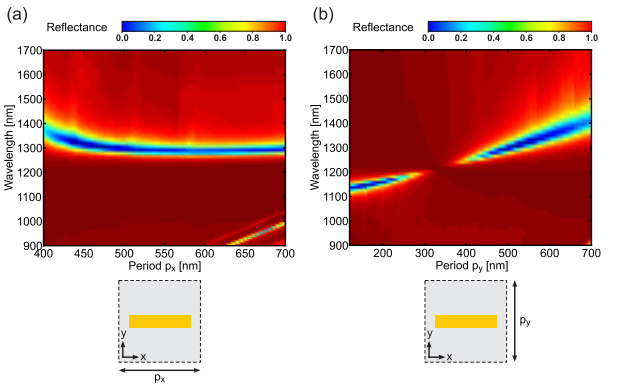

Figure 35 Reflectance plots of the combined cavity-nanorod structure for different periods in (a) x-direction and (b) y-direction.

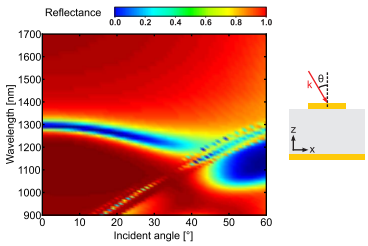

Figure 36 Reflectance plots of the combined cavity-nanorod structure for different incident angles θ.

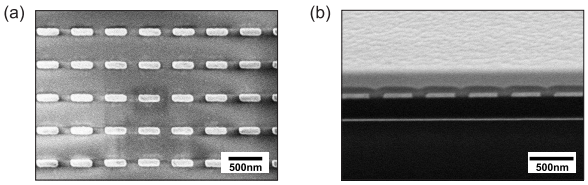

Figure 37 © American Institute of Physics [84]. (a) Top view and (b) side view of the cavity sensing structure. For the side view, a hole was cut in the structure using a focussed ion beam. A protection layer had to be evaporated for the cut which is visible above the nanorods.

Figure 38 The microfluidic sensing cell [16].

4.4. Experimental Results

4.4.1. Sample Fabrication

The sample was fabricated using thermal evaporation for the gold layers, spin-coating for the dielectric spacer, and electron-beam lithography for the nanostructuring. The thickness of the lower gold layer is 40 nm. The material of the dielectric spacer is the polysiloxane-based spin-on glass IC1-200 with a refractive index of $n_{IC1} = 1.40$ and a layer thickness of 380 nm. The nanorods have a thickness of 70 nm, a length of 380 nm, and a width of 100 nm. The unit cell size of the nanorod array is 500 nm × 500 nm which is well below the distance where Rayleigh- or Wood-anomalies cause problems [108]. The total size of the nanorod array is 100 µm × 100 µm. Fig. 37 shows SEM images providing a top and a side view on the structure. For comparative measurements, the same nanorod array was also fabricated without the cavity directly on a glass substrate.

4.4.2. Experimental Setup

The method of enhancing the sensitivity S^* and the figures of merit FOM and FOM^* of a plasmonic sensor was experimentally demonstrated using water and glucose solutions. Using a microfluidic sensing cell [16] attached to a number of syringes, the different liquids were channeled over the sample. The cell [Fig. 38] consists of a metallic sample substrate holder and two layers made of PDMS (polydimethylsiloxane) and polycarbonate directing the liquids from the fluid connectors to the sample surface via 80 µm thin channels. The spectra were measured at opening angles from 10° to 24° with a FTIR-spectrometer and an attached infrared microscope.

4.4.3. Measured Spectra

In Fig. 39, the simulated and experimental spectra for both bare nanorods and nanorods combined with the cavity are compared. The shifts of the resonances for the nanorods surrounded by water ($n_1 = 1.3198$ [109]) and by a 25%-solution of glucose in water ($n_2 = 1.3594$ [110]) can be observed. The refractive index change is hence $\Delta n = n_2 - n_1 = 0.0396$. The refractive indices of the liquids are taken at a wavelength of 1300 nm. The decrease of the resonance linewidth when the cavity is added to the nanorods is very distinct. The linewidth of the peak decreases drastically from 900 nm to 50 nm in simulation and from 600 nm to 90 nm in experiment. In order to accurately compare both structures, the configuration with the best FOM^* was used, which is the detection of transmittance for the nanorods alone and the detection of reflectance for the nanorods combined with the cavity.

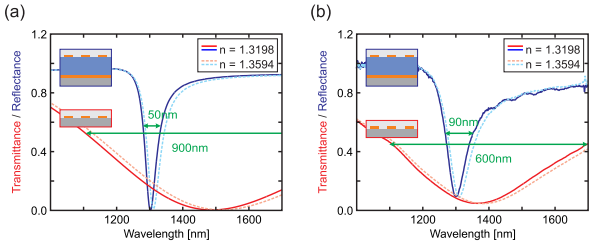

Figure 39 © American Institute of Physics [84]. (a) Simulated and (b) experimental spectra of bare nanorods (red curves) compared to nanorods combined with a cavity (blue curves) for liquids with two different refractive indices surrounding the nanorods.

4.4.4. Sensitivity and Figure of Merit

From the spectra and the refractive index difference, the sensitivities and figures of merit (Eqs. 13 to 16) can be calculated. The values for the calculated sensitivity S and figure of merit FOM as well as the maximum values for the sensitivity S^* and the figure of merit FOM^* are summed up in Tab. 4 both for simulated and measured data from nanorods alone and from nanorods combined with a cavity.

It turns out that the sensitivity $S = \Delta\lambda/\Delta n$ actually decreases by a factor of 2.5 in simulations and 2.3 in experiments when the cavity is added to the nanorods. This is likely due to the fact that the mode volume increases due to the cavity. Nevertheless, since the linewidth of the peak decreases drastically, the figure of merit $FOM = S/FWHM$ increases by a factor of 7.1 in simulations and by a factor of 3.1 in the experimental measurement. The small linewidth has also a large effect on the sensitivity S^* since a small shift causes a high variation in the reflected intensity. The observed increase for the maximum sensitivity $S^*_{\max}$ is 5.5 in simulation and 3.7 in experiment. At the minimum, the

Structure	Nanorods alone	Nanorods + Cavity	Enhancement factor
$\Delta\lambda$	35 nm (27 nm)	14 nm (12 nm)	0.4 (0.4)
S	884 nm/RIU (682 nm/RIU)	354 nm/RIU (303 nm/RIU)	0.4 (0.4)
FOM	1.0 (1.1)	7.1 (3.4)	7.1 (3.1)
$S^*_{\max}$	1.1 (0.9)	6.1 (3.3)	5.5 (3.7)
$FOM^*_{\max}$	47 (5.9)	$\to\infty$ (20.8)	$\to\infty$ (3.5)

Table 4 Summary of the determined sensitivities and figures of merit. The values in brackets denote the experimental values.

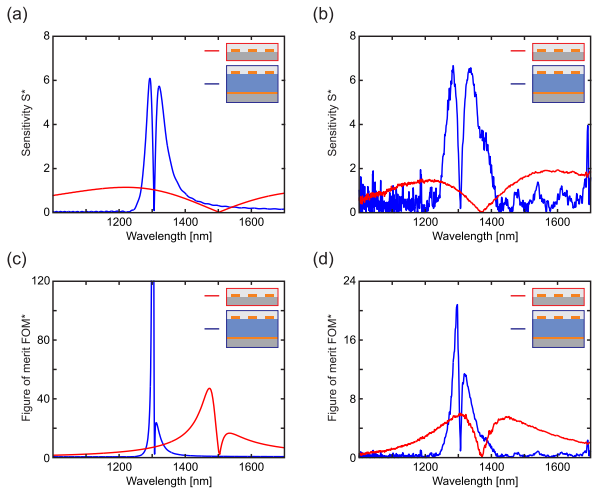

Figure 40 © American Institute of Physics [84]. (a, b) Sensitivity S^* and (c, d) figure of merit FOM^* for different wavelengths determined from the (a, c) simulated and (b, d) measured spectra. Red curves correspond to nanorods alone, blue curves to nanorods combined with a cavity.

fraction of the reflected light intensity is only 9%, resulting in an enhancement factor of 3.5 for the measured figure of merit FOM^*. In the simulations, zero reflected intensity at the resonance of the cavity results in a theoretically infinite value for FOM^*. The dependence of S^* and FOM^* on the wavelength is plotted in Fig. 40. The shape of the curves of S^* and FOM^* (two close maxima and a minimum in between with a kink at 0) originates from the fact that $\Delta I = 0$ where the curves for the two different liquids intersect, whereas close by, the slope increases ($\Rightarrow$ large S^*) and the absolute intensity is still very low ($\Rightarrow$ large FOM^*). The deviations between simulated and experimental values are most likely due to fabrication imperfections and non-normal light inicidence.

5. Comparison with other plasmonic systems

In comparison to the here investigated photonic microcavities that are coupled to localized or propagating surface plasmons, recent literature shows a lot of papers on plasmonic cavities. In most of these numerous cases, the metallic nanostructure itself acts as the resonator in which the plasmon resonates in a propagating or localized fashion.

We would like to mention the following examples: A first paper by G. Gantzounis et al. [111] discusses a chain of spherical voids in a metallic bulk environment. Complementary to the metal nanoparticle chain of Brongersma and Maier and coworkers [15, 32], in that work the dispersion relation of propagating waves was calculated, and group velocities on the order of 0.1 c were predicted.

In 2006, J. Dionne published experimental results on metal-insulator-metal (MIM) slot waveguides, which resemble a sub-wavelength Fabry-Pérot cavity [112]. Propagation distances using the coupled surface plasmon modes at the metal-air interface of 5 wavelengths at a simultaneous field confinement of $\lambda/5$ were reported. V. Sorger et al. realized an all-plasmonic nanocavity consisting of a MIM geometry with a Q-factor of up to 200 in the visible wavelength range [47]. M. Bora et al. reported on a similar geometry, using two parallel plasmonic nanowires with a subwavelength gap inbetween [113]. A confinement factor of 10^3 was reported.

A different approach was brought forward by the group of J. Vuckovic, who designed a plasmonic cavity using corrugated metal layers with defects in periodicity on GaAs to predict Q-factors of 1000 and Purcell enhancement of 100 [114]. In a different geometry, K. J. Russell and E. L. Hu reported experimental Q-factors of 30 to 60 in a cavity consisting of a silver nanowire over a silver surface with PbS dots in the 15 nm gap [115].

In a pioneering ansatz, M. Hill reported a metal clad vertical nanolaser, where a 200 nm wide InGaAs post was surrounded by silver or gold and lased upon electrically pumping at low temperatures [116]. Their Q-factor was on the order of 140 to 200.

Coupled microcavities covered with metals have been reported by R. Perahia [48] and B. Min [117]. In the first case, a micropillar microcavity reached a simulated Q-factor of up to 4000 and was brought to room temperature lasing at 1.3 µm wavelength. They studied particularly the mode hybridization between the surface plasmon and the whispering gallery mode. In the second case, a silica microcavity of roughly 20 µm diameter was coated with silver, and experimental Q-factors of 1375 were reported around 1.5 µm wavelength at room temperature.

6. Conclusions

6.1. Summary

We provided an investigation of the plasmon-plasmon as well as the light-plasmon coupling strength and range in multilayer nanostructures and demonstrated the manipulation of the plasmon resonances by modifying the environment using microcavities. Different models, such as the dipole model, image charges, and plasmon hybridization as well as a consideration of phase shifts and the assignment of effective resonant permittivities were used to explain the observed behavior of near- and far-field coupled nanostructures.

In analogy to the strong coupling of atoms or quantum dots to photonic cavity modes, it was demonstrated that also localized plasmons and propagating surface plasmons can be coupled strongly to light. In particular, it was shown that either the symmetric (electric) or the antisymmetric (magnetic) hybridized plasmon modes of nanorod pairs can exhibit strong coupling to standing waves in a microcavity depending on the position of the nanostructure in the cavity. The behavior is explained by the direction of the electric field vectors of the resonator modes at the positions of the nanorods. The splitting can be as large as 82 meV for the magnetic and 354 meV for the electric mode which is very large, as the splitting is 36% of the resonance energy. The experimentally observed splitting-to-linewidth ratio can be as large as 10 for the symmetric (electric) mode and 2.5 for the antisymmetric (magnetic) plasmon mode. Especially the coupling strength to the magnetic dipole of the antisymmetric mode is remarkable since magnetic moments usually can not be addressed easily.

The concept was extended from localized plasmons to propagating surface plasmons. Surface plasmons can only be excited under certain conditions that can be met by placing an array of continuous nanowires close to a mirror. The creation of a microcavity by positioning a second mirror at an appropriate distance allowed the strong coupling of the photonic cavity modes to the surface plasmons. The measured splitting energies were in the range of 10% of the resonance energy. It was shown that the cavity modes can also mediate a coupling of localized and surface plasmons via far-field distances.

The excellent agreement between the simulations and the measured spectra of the various fabricated samples required accurate and versatile fabrication procedures for the multilayer nanostructures. It was demonstrated that different thin layer and nanostructure fabrication techniques can

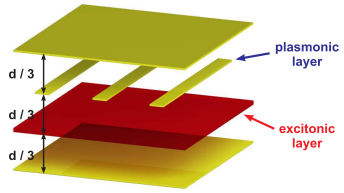

Figure 41 Microcavities can be used to couple excitons and plasmons via the far-field. Excitonic resonances can be excited for example in a layer of quantum dots or J-aggregates.

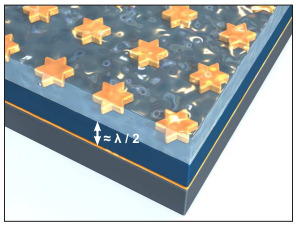

Figure 42 Many kinds of geometries of sensitive nanostructures, such as nanostars, can be combined with a microcavity to enhance their sensing properties.

be combined to produce the functional nanostructures in a layer-by-layer fashion. A combination of spin-on glasses and evaporated dielectric materials was used to produce spacer layers of a wide range of thicknesses with well-defined parameters. Furthermore, it was shown that the very simple technique of applying mechanical pressure on two substrates is suitable for the construction of microcavities with a variable resonator length ranging from several micrometers to only a few hundred nanometers.

The acquired knowledge of the coupling mechanisms and fabrication procedures of the considered structures was used to design a structure for a practical application. A method to enhance the sensing properties of a localized plasmon sensor was investigated theoretically and experimentally. It was shown that the technique of adding a mirror at an appropriate distance to a sensitive nanostructure and thereby creating a cavity can considerably increase the sensitivity due to an extremely decreased linewidth of the coupled plasmonic-photonic resonance. The values characterizing the properties of an LSPR sensor could be increased by a factor of more than 3 in the experiments. Furthermore, an overview of different parameters to characterize a sensor was given since the assignment of a mere sensitivity defined as the resonance shift per refractive index unit change is not sufficient to fully describe and compare sensors.

6.2. Outlook

In general, the concepts can be further expanded to multiple cavities or multiple elements at Bragg- or anti-Bragg spacing. At the end of Chs. 1 and 2, the properties of multilayer stacks were briefly examined. The investigation of plasmon far-field coupling mechanisms are important in the context of three-dimensional novel materials with unconventional optical properties (3D-metamaterials) consisting of many nanostructured layers. An increase in coupling strength and range can facilitate the production and improve the functionality of these materials. Also, the indication of band gap formation in Bragg-spaced multilayer nanostructures already at a very small number of layers can be used for functional layers with tailored transmission and reflection properties that are applicable as nanoscale filters or absorbers for example in integrated optics.

Even more intriguing is the coupling to quantum emitters, such as J-aggregates or semiconductor quantum dots [Fig. 41], which can be spaced a Bragg distance away from the metal. J-aggregates are coupled dye molecules exhibiting sharp excitonic resonances [118–120]. The far-field coupling of excitons and plasmons in microcavities avoids near-field quenching and should result in strongly coupled plasmon/exciton states, i.e., plexcitons [56].

The highlighted sensing applications of strongly coupled plasmonic and photonic modes in Ch. 4 can be further improved in a number of ways: At first, the cavity volume can be included for the sensing by different methods such as using porous media in the cavity, placing the nanostructures on pillars by drilling or etching holes or channels in the cavity or using microfluidic techniques. Second, a functionalization of the nanostructures can specialize the sensor and make it sensitive for certain kind of substances. Furthermore, the concept can be applied to many LSPR sensor structures superior to nanorods [98, 121], e.g., colloidal systems such as nanostars (Fig. 42), and will considerably improve their sensing properties. In general, the coupling in microcavities might be further increased by using dielectric mirrors resulting in high-Q cavities. Recently, it has been demonstrated that whispering-gallery modes can be used to enhance the plasmon resonance shift in biosensors by a factor of 4 [122]. Potential applications of LSPR sensing in the fields of biotechnology, medical diagnostics, or pharmacology including biomolecule detection as well as real-time monitoring of chemical reactions or molecular kinetics might benefit from this concept.

Acknowledgements.

We would like to thank R. Taubert for useful discussions, B. Fenk and U. Eigenthaler for the focused ion beam support, M. Hentschel and D. Dregely for sample fabrications, and M. Mesch for glucose sensing assistance. We acknowledge financial support from the Deutsche Forschungsgemeinschaft (FOR557, SPP1391) and the Bundesministerium für Bildung und Forschung (13N10146, 13N9049).

Key words: Plasmonics, Microcavity, Coupling

Dr. Ralf Ameling studied Physics at the University of Ulm and received his Diploma in 2007. In 2011 he obtained his PhD from the University of Stuttgart at the 4th Physics Institute. His research interests include the design, fabrication and characterization of three-dimensional metallic nanostructures. In particular, his research is concerned with the coupling of plasmons and light in microcavities and its applications.

Prof. Dr. Harald Giessen is a Professor of Experimental Physics at the University of Stuttgart, Germany. He is the director of the 4th Physics Institute and directs the Nanostructure Laboratory of the Department of Physics. His research area is ultrafast nanooptics, focusing on plasmonics, metallic photonic crystals, metamaterials, and their linear and nonlinear optical properties in the visible and near-infrared wavelength range. In particular, he is interested in three-dimensional geometries, including 3D metamaterials, cavity geometries, and Bragg stacking. His applications are geared towards novel plasmonic sensing schemes.

References

[1] J. Valentine, S. Zhang, T. Zentgraf, E. Ulin-Avila, D. A. Genov, G. Bartal, and X. Zhang, Nature **455**, 376 (2008).
[2] J. Pendry, Phys. Rev. Lett. **85**, 3966 (2000).
[3] J. B. Pendry, D. Schurig, and D. R. Smith, Science **312**, 1780 (2006).
[4] T. Ergin, N. Stenger, P. Brenner, J. B. Pendry, and M. Wegener, Science **328**, 337 (2010).
[5] P. Mühlschlegel, H. J. Eisler, O. J. F. Martin, B. Hecht, and D. W. Pohl, Science **308**, 1607 (2005).
[6] P. J. Schuck, D. P. Fromm, A. Sundaramurthy, G. S. Kino, and W. E. Moerner, Phys. Rev. Lett. **94**, 017402 (2005).
[7] D. Dregely, R. Taubert, J. Dorfmüller, R. Vogelgesang, K. Kern, and H. Giessen, Nature Commun. **2**, 267 (2011).
[8] R. Zia, J. Schuller, A. Chandran, and M. Brongersma, Materials Today **9**, 20 (2006).
[9] D. Bergman and M. Stockman, Phys. Rev. Lett. **90**, 027402 (2003).
[10] R. F. Oulton, V. J. Sorger, T. Zentgraf, R. M. Ma, C. Gladden, L. Dai, G. Bartal, and X. Zhang, Nature **461**, 629 (2009).
[11] K. A. Willets and R. P. Van Duyne, Annu. Rev. Phys. Chem. **58**, 267 (2007).
[12] S. Lal, S. Link, and N. J. Halas, Nature Phot. **1**, 641 (2007).
[13] J. N. Anker, W. P. Hall, O. Lyandres, N. C. Shah, J. Zhao, and R. P. Van Duyne, Nature Mater. **7**, 442 (2008).
[14] N. Liu, H. Guo, L. Fu, S. Kaiser, H. Schweizer, and H. Giessen, Nature Mater. **7**, 31 (2008).
[15] S. A. Maier, P. G. Kik, H. A. Atwater, S. Meltzer, E. Harel, B. E. Koel, and A. G. Requicha, Nature Mater. **2**, 229 (2003).
[16] N. Liu, T. Weiss, M. Mesch, L. Langguth, U. Eigenthaler, M. Hirscher, C. Sönnichsen, and H. Giessen, Nano Lett. **10**, 1103 (2010).
[17] V. A. Podolskiy, A. K. Sarychev, and V. M. Shalaev, J. Nonlinear Opt. Phys. **11**, 65 (2002).
[18] G. Dolling, C. Enkrich, M. Wegener, J. F. Zhou, C. M. Soukoulis, and S. Linden, Opt. Lett. **30**, 3198 (2005).
[19] A. Christ, Y. Ekinci, H. Solak, N. Gippius, S. Tikhodeev, and O. Martin, Phys. Rev. B **76**, 201405(R) (2007).
[20] A. Christ, O. J. F. Martin, Y. Ekinci, N. A. Gippius, and S. G. Tikhodeev, Nano Lett. **8**, 2171 (2008).
[21] G. Dolling, C. Enkrich, M. Wegener, C. M. Soukoulis, and S. Linden, Science **312**, 892 (2006).
[22] N. Liu, L. Fu, S. Kaiser, H. Schweizer, and H. Giessen, Adv. Mater. **20**, 3859 (2008).
[23] N. Liu, S. Kaiser, and H. Giessen, Adv. Mater. **20**, 4521 (2008).
[24] N. Liu and H. Giessen, Angew. Chemie Int. Ed. **49**, 9838 (2010).
[25] S. A. Maier, P. G. Kik, and H. A. Atwater, Appl. Phys. Lett. **81**, 1714 (2002).
[26] H. Liu, D. A. Genov, D. M. Wu, Y. M. Liu, J. M. Steele, C. Sun, S. N. Zhu, and X. Zhang, Phys. Rev. Lett. **97**, 243902 (2006).
[27] M. Hentschel, M. Saliba, R. Vogelgesang, H. Giessen, A. P. Alivisatos, and N. Liu, Nano Lett. **10**, 2721 (2010).
[28] Y. A. Urzhumov, G. Shvets, J. A. Fan, F. Capasso, D. Brandl, and P. Nordlander, Opt. Express **15**, 14129 (2007).
[29] J. A. Fan, C. Wu, K. Bao, J. Bao, R. Bardhan, N. J. Halas, V. N. Manoharan, P. Nordlander, G. Shvets, and F. Capasso, Science **328**, 1135 (2010).
[30] A. Alù and N. Engheta, Phys. Rev. Lett. **104**, 213902 (2010).
[31] L. Zhao, K. L. Kelly, and G. C. Schatz, J. Phys. Chem. B **107**, 7343 (2003).
[32] S. A. Maier, M. L. Brongersma, P. G. Kik, and H. A. Atwater, Phys. Rev. B **65**, 193408 (2002).
[33] L. Langguth and H. Giessen, Opt. Express (2011, in press).
[34] E. Prodan, C. Radloff, N. J. Halas, and P. Nordlander, Science **302**, 419 (2003).
[35] P. Nordlander, C. Oubre, E. Prodan, K. Li, and M. I. Stockman, Nano Lett. **4**, 899 (2004).
[36] V. A. Podolskiy, A. K. Sarychev, E. E. Narimanov, and V. M. Shalaev, J. Opt. A: Pure Appl. Opt. **7**, 32 (2005).
[37] C. Enkrich, M. Wegener, S. Linden, S. Burger, L. Zschiedrich, F. Schmidt, J. Zhou, T. Koschny, and C. Soukoulis, Phys. Rev. Lett. **95**, 203901 (2005).
[38] T. P. Meyrath, T. Zentgraf, C. Rockstuhl, and H. Giessen, Appl. Phys. B **93**, 107 (2008).
[39] S. Tretyakov, Analytical Modeling in Applied Electromagnetics (Artech, 2003).

[40] P. B. Johnson and R. W. Christy, Phys. Rev. B **6**, 4370 (1972).
[41] M. L. Thèye, Phys. Rev. B **2**, 3060 (1970).
[42] M. A. Ordal, L. L. Long, R. J. Bell, S. E. Bell, R. R. Bell, R. W. Alexander Jr., and C. A. Ward, Appl. Opt. **22**, 1099 (1983).
[43] N. Liu, H. Guo, L. Fu, S. Kaiser, H. Schweizer, and H. Giessen, Adv. Mater. **19**, 3628 (2007).
[44] R. Taubert, R. Ameling, T. Weiss, A. Christ, and H. Giessen, Nano Lett. **11**, 4421 (2011).
[45] M. Scalora, M. J. Bloemer, A. S. Pethel, J. P. Dowling, C. M. Bowden, and A. S. Manka, J. Appl. Phys. **83**, 2377 (1998).
[46] R. Taubert, D. Dregely, A. Christ, and H. Giessen(2011, submitted).
[47] V. J. Sorger, R. F. Oulton, J. Yao, G. Bartal, and X. Zhang, Nano Lett. **9**, 3489 (2009).
[48] R. Perahia, T. P. M. Alegre, A. H. Safavi-Naeini, and O. Painter, Appl. Phys. Lett. **95**, 201114 (2009).
[49] J. Parsons, I. R. Hooper, W. L. Barnes, and J. R. Sambles, J. Mod. Opt. **56**, 1199 (2009).
[50] M. Barth, S. Schietinger, S. Fischer, J. Becker, N. Nüsse, T. Aichele, B. Löchel, C. Sönnichsen, and O. Benson, Nano Lett. **10**, 891 (2010).
[51] H. Altug, D. Englund, and J. Vuckovic, Nature Phys. **2**, 484 (2006).
[52] R. M. Ma, R. F. Oulton, V. J. Sorger, G. Bartal, and X. Zhang, Nature Mater. **10**, 110 (2011).
[53] R. J. Thompson, G. Rempe, and H. J. Kimble, Phys. Rev. Lett. **68**, 1132 (1992).
[54] K. H. Drexhage, Prog. Optics **12**, 163 (1974).
[55] J. Dintinger, S. Klein, F. Bustos, W. L. Barnes, and T. W. Ebbesen, Phys. Rev. B **71**, 035424 (2005).
[56] N. T. Fofang, T. H. Park, O. Neumann, N. A. Mirin, P. Nordlander, and N. J. Halas, Nano Lett. **8**, 3481 (2008).
[57] T. K. Hakala, J. J. Toppari, A. Kuzyk, M. Pettersson, H. Tikkanen, H. Kunttu, and P. Törmä, Phys. Rev. Lett. **103**, 053602 (2009).
[58] C. Weisbuch, M. Nishioka, A. Ishikawa, and Y. Arakawa, Phys. Rev. Lett. **69**, 3314 (1992).
[59] P. Meystre, Prog. Optics **30**, 261 (1992).
[60] G. Khitrova, H. M. Gibbs, F. Jahnke, M. Kira, and S. W. Koch, Rev. Mod. Phys. **71**, 1591 (1999).
[61] S. M. Ulrich, C. Gies, S. Ates, J. Wiersig, S. Reitzenstein, C. Hofmann, A. Löffler, A. Forchel, F. Jahnke, and P. Michler, Phys. Rev. Lett. **98**, 043906 (2007).
[62] J. P. Reithmaier, G. Sek, A. Löffler, C. Hofmann, S. Kuhn, S. Reitzenstein, L. V. Keldysh, V. D. Kulakovskii, T. L. Reinecke, and A. Forchel, Nature **432**, 197 (2004).
[63] T. Yoshie, A. Scherer, J. Hendrickson, G. Khitrova, H. M. Gibbs, G. Rupper, C. Ell, O. B. Shchekin, and D. G. Deppe, Nature **432**, 200 (2004).
[64] M. Hübner, J. Kuhl, T. Stroucken, A. Knorr, S. W. Koch, R. Hey, and K. Ploog, Phys. Rev. Lett. **76**, 4199 (1996).
[65] M. Hübner, J. P. Prineas, C. Ell, P. Brick, E. S. Lee, G. Khitrova, H. M. Gibbs, and S. W. Koch, Phys. Rev. Lett. **83**, 2841 (1999).
[66] R. Ameling and H. Giessen, Nano Lett. **10**, 4394 (2010).
[67] V. M. Shalaev, Nature Phot. **1**, 41 (2007).
[68] C. M. Soukoulis, S. Linden, and M. Wegener, Science **315**, 47 (2007).
[69] J. Zhou, T. Koschny, M. Kafesaki, and C. M. Soukoulis, Phys. Rev. B **80**, 035109 (2009).
[70] A. Boca, R. Miller, K. M. Birnbaum, A. D. Boozer, J. McKeever, and H. J. Kimble, Phys. Rev. Lett. **93**, 233603 (2004).
[71] E. Peter, P. Senellart, D. Martrou, A. Lematre, J. Hours, J. M. Gerard, and J. Bloch, Phys. Rev. Lett. **95**, 067401 (2005).
[72] G. Khitrova, H. M. Gibbs, M. Kira, S. W. Koch, and A. Scherer, Nature Phys. **2**, 81 (2006).
[73] D. Lu, H. Liu, T. Li, S. M. Wang, F. M. Wang, S. N. Zhu, and X. Zhang, Phys. Rev. B **77**, 214302 (2008).
[74] R. Ameling, D. Dregely, and H. Giessen, Opt. Lett. **36**, 2218 (2011).
[75] J. Cesario, R. Quidant, G. Badenes, and S. Enoch, Opt. Lett. **30**, 3404 (2005).
[76] W. Holland and D. Hall, Phys. Rev. Lett. **52**, 1041 (1984).
[77] W. Holland and D. Hall, Phys. Rev. B **27**, 7765 (1983).
[78] A. Christ, T. Zentgraf, S. G. Tikhodeev, N. A. Gippius, J. Kuhl, and H. Giessen, Phys. Rev. B **74**, 155435 (2006).
[79] D. M. Whittaker and I. S. Culshaw, Phys. Rev. B **60**, 2610 (1999).
[80] S. G. Tikhodeev, A. L. Yablonskii, E. A. Muljarov, N. A. Gippius, and T. Ishihara, Phys. Rev. B **66**, 045102 (2002).
[81] T. Weiss, N. A. Gippius, S. G. Tikhodeev, G. Granet, and H. Giessen, J. Opt. A: Pure Appl. Opt. **11**, 114019 (2009).
[82] E. Feigenbaum and M. Orenstein, Phys. Rev. Lett. **101**, 163902 (2008).
[83] J. Dorfmüller, R. Vogelgesang, R. T. Weitz, C. Rockstuhl, C. Etrich, T. Pertsch, F. Lederer, and K. Kern, Nano Lett. **9**, 2372 (2009).
[84] R. Ameling, L. Langguth, M. Hentschel, M. Mesch, P. V. Braun, and H. Giessen, Appl. Phys. Lett. **97**, 253116 (2010).
[85] A. J. Haes, L. Chang, W. L. Klein, and R. P. Van Duyne, J. Am. Chem. Soc. **127**, 2264 (2005).
[86] H. Liao, C. L. Nehl, and J. H. Hafner, Nanomedicine **1**, 201 (2006).
[87] K. M. Byun, J. Opt. Soc. Korea **14**, 65 (2010).
[88] A. A. Yanik, M. Huang, A. Artar, T. Y. Chang, and H. Altug, Appl. Phys. Lett. **96**, 021101 (2010).
[89] G. Mattei, P. Mazzoldi, M. L. Post, D. Buso, M. Guglielmi, and A. Martucci, Adv. Mater. **19**, 561 (2007).
[90] D. Nau, A. Seidel, R. B. Orzekowsky, S. H. Lee, S. Deb, and H. Giessen, Opt. Lett. **35**, 3150 (2010).
[91] E. M. Larsson, C. Langhammer, I. Zorić, and B. Kasemo, Science **326**, 1091 (2009).
[92] N. J. Halas, Nano Lett. **10**, 3816 (2010).
[93] J. J. Mock, D. R. Smith, and S. Schultz, Nano Lett. **3**, 485 (2003).
[94] J. Becker, A. Trügler, A. Jakab, U. Hohenester, and C. Sönnichsen, Plasmonics **5**, 161 (2010).
[95] A. J. Haes and R. P. Van Duyne, J. Am. Chem. Soc. **124**, 10596 (2002).
[96] N. Nath and A. Chilkoti, Anal. Chem. **74**, 504 (2002).
[97] J. Homola, Sensor. Actuat. B: Chem. **54**, 3 (1999).
[98] H. Chen, X. Kou, Z. Yang, W. Ni, and J. Wang, Langmuir **24**, 5233 (2008).
[99] L. J. Sherry, S. H. Chang, G. C. Schatz, R. P. Van Duyne, B. J. Wiley, and Y. Xia, Nano Lett. **5**, 2034 (2005).
[100] N. Liu, M. Mesch, T. Weiss, M. Hentschel, and H. Giessen, Nano Lett. **10**, 2342 (2010).
[101] C. Sönnichsen, T. Franzl, T. Wilk, G. von Plessen, and J. Feldmann, Phys. Rev. Lett. **88**, 077402 (2002).

[102] N. Liu, L. Langguth, T. Weiss, J. Kästel, M. Fleischhauer, T. Pfau, and H. Giessen, Nature Mater. **8**, 758 (2009).
[103] J. B. Lassiter, H. Sobhani, J. A. Fan, J. Kundu, F. Capasso, P. Nordlander, and N. J. Halas, Nano Lett. **10**, 3184 (2010).
[104] S. Zhang, D. A. Genov, Y. Wang, M. Liu, and X. Zhang, Phys. Rev. Lett. **101**, 047401 (2008).
[105] R. D. Kekatpure, E. S. Barnard, W. Cai, and M. L. Brongersma, Phys. Rev. Lett. **104**, 243902 (2010).
[106] A. Artar, A. A. Yanik, and H. Altug, Appl. Phys. Lett. **95**, 051105 (2009).
[107] M. Huang, A. A. Yanik, T. Y. Chang, and H. Altug, Opt. Express **17**, 24224 (2009).
[108] A. Christ, T. Zentgraf, J. Kuhl, S. G. Tikhodeev, N. A. Gippius, and H. Giessen, Phys. Rev. B **70**, 125113 (2004).
[109] J. E. Bertie and Z. Lan, Appl. Spectrosc. **50**, 1047 (1996).
[110] Y. L. Yeh, Opt. Laser. Eng. **46**, 666 (2008).
[111] G. Gantzounis and N. Stefanou, Phys. Rev. B p. 085102.
[112] J. A. Dionne, H. J. Lezec, and H. A. Atwater, Nano Lett. **6**, 1928 (2006).
[113] M. Bora, B. J. Fasenfest, E. M. Behymer, A. S. P. Chang, H. T. Nguyen, J. A. Britten, C. C. Larson, J. W. Chan, R. R. Miles, and T. C. Bond, Nano Lett. **10**, 2832 (2010).
[114] Y. Gong and J. Vuckovic, Appl. Phys. Lett. **90**, 033113 (2007).
[115] K. J. Russell and E. L. Hu, Appl. Phys. Lett. **97**, 163115 (2010).
[116] M. T. Hill, Y. S. Oei, B. Smalbrugge, Y. Zhu, T. de Vries, P. J. van Veldhoven, F. W. M. van Otten, T. J. Eijkemans, J. P. Turkiewicz, H. de Waardt, E. J. Geluk, S. H. Kwon, Y. H. Lee, R. Notzel, and M. K. Smit, Nature Phot. **1**, 589 (2007).
[117] B. Min, E. Ostby, V. Sorger, E. Ulin-Avila, L. Yang, X. Zhang, and K. Vahala, Nature **457**, 455 (2009).
[118] G. Scheibe, Angew. Chem. **50**, 212 (1937).
[119] E. E. Jelley, Nature **138**, 1009 (1936).
[120] D. Möbius, Adv. Mater. **7**, 437 (1995).
[121] R. Alvarez-Puebla, L. M. Liz-Marzán, and F. J. García De Abajo, J. of Phys. Chem. Lett. **1**, 2428 (2010).
[122] S. I. Shopova, R. Rajmangal, S. Holler, and A. Arnold, Appl. Phys. Lett. **98**, 243104 (2011).